

<sup>1</sup> An optimal volumetric constraint ratio with  
<sup>2</sup> implementation using mixed FE-Meshfree formulation

<sup>3</sup> Wu Junchao<sup>a,\*</sup>, Chu Yingjie<sup>1</sup>, Xu Yangtao<sup>a</sup>, Wang Dongdong<sup>1</sup>

<sup>a</sup> Key Laboratory for Intelligent Infrastructure and Monitoring of Fujian Province, College  
of Civil Engineering, Huaqiao University, Xiamen, Fujian, 361021, China

---

<sup>4</sup> **Abstract**

Formulations for incompressible materials often suffer from volumetric locking, leading to reduced accuracy and oscillatory displacement and pressure solutions. A well-chosen constraint ratio can mitigate this issue, but traditional approaches lack a theoretical foundation based on the inf-sup (or LBB) condition, which is essential for the stability of mixed formulations. This paper introduces a novel optimal constraint ratio derived from the inf-sup condition to address volumetric locking. The inf-sup test, a numerical tool for verifying the inf-sup condition, is reaffirmed as equivalent to the inf-sup condition through a variational approach. By incorporating a complete polynomial space whose dimension matches the number of displacement degrees of freedom (DOFs), a new inf-sup value estimator is developed, explicitly considering the constraint ratio. For a given number of displacement DOFs, ensuring that the pressure DOFs remain below a stabilized number falls within the optimal constraint ratio range can satisfy the inf-sup condition. To implement the optimal constraint ratio, a mixed finite element and meshfree formulation is proposed, where displacements are discretized using traditional finite element approximations, and pressures are approximated via the reproducing kernel meshfree method. Leveraging the globally smooth reproducing kernel shape functions, the constraint ratio can be flexibly adjusted to meet the inf-sup condition without the limit of element. For computational efficiency and ease of implementation, pressure nodes are placed on selected displacement nodes to maintain the optimal constraint ratio. Inf-sup tests and a series of 2D and 3D elasticity examples validate the proposed constraint ratio, demonstrating its effectiveness in eliminating volumetric locking and enhancing the performance of mixed finite element and meshfree formulations.

<sup>5</sup> **Keywords:** Optimal constraint ratio, Inf-sup condition estimator, Volumetric  
<sup>6</sup> locking, Mixd formulation, Reproducing kernel meshfree approximation

---

---

\*Corresponding author  
Email address: jcwu@hqu.edu.cn (Wu Junchao)

7      **1. Introduction**

8      The volumetric constraint is a necessary condition in the formulation of  
 9      incompressible materials like rubber and hydrogel. Proper imposition of this  
 10     constraint is crucial for obtaining better numerical solutions; insufficient or ex-  
 11     cessive constraints will reduce the accuracy and stability of the solution [1]. The  
 12     volumetric constraint ratio [2], denoted as  $r$ , is often used to measure the level  
 13     of constraint. It is defined as the total degrees of freedom (DOFs) of displace-  
 14     ment divided by the total DOFs of pressure. Ideally, the optimal constraint  
 15     ratio should be consistent with its governing partial differential equations. For  
 16     example, in the two-dimensional (2D) case, the optimal constraint ratio is 2,  
 17     since there are two governing equations for displacement and one for pressure.  
 18     When the constraint ratio is less than 2, the formulation suffers from volumetric  
 19     locking, while a constraint ratio greater than 2 can cause a coarse solution for  
 20     pressure. These observations have been summarized by pioneering work [2] as  
 21     follows:

$$r = \frac{2n_u}{n_p}, \quad \begin{cases} r > 2 & \text{too few constraints} \\ r = 2 & \text{optimal} \\ r < 2 & \text{too many constraints} \\ r \leq 1 & \text{severe locking} \end{cases} \quad (1)$$

22     where  $n_u$  and  $n_p$  are the number of control nodes for displacement and pressure,  
 23     respectively. Classifying the locked status via the constraint ratio is straight-  
 24     forward but imprecise. For instance, the constraint ratio can remain 2 while  
 25     the pressure is discretized using continuous shape functions identical to the  
 26     displacement's approximation. However, volumetric locking still exists in this  
 27     formulation [2].

28     The inf-sup condition, also known as the Ladyzhenskay–Babuška–Brezzi  
 29     (LBB) condition [3, 4], is a more precise requirement for a locking-free for-  
 30     mulation. This condition is based on the mixed formulation framework, and  
 31     when the inf-sup condition is satisfied, both the accuracy and stability of the  
 32     mixed-formulation can be ensured. However, verifying the inf-sup condition is  
 33     non-trivial. An eigenvalue problem namely inf-sup test can be used to check  
 34     this condition numerically [5, 6, 7, 8]. Analytically, Brezzi and Fortin proposed  
 35     a two-level projection framework that always satisfies the inf-sup condition, al-  
 36     lowing it to be checked by identifying whether the formulation is included in  
 37     this framework. Both analytical and numerical methods to check the inf-sup  
 38     condition are complex, and the relationship between the constraint ratio and  
 39     the inf-sup condition remains unclear.

40     To address volumetric constraint issues, adjusting the constraint ratio to an  
 41     appropriate level is commonly used and easily implemented. In traditional finite  
 42     element methods (FEM), this adjustment is carried out based on elements since  
 43     the DOFs are embedded in each element. Conventional FEM often exhibits  
 44     an over-constrained status. Reducing the approximation order of pressure in  
 45     mixed formulation can alleviate the constraint burden, such as with the well-  
 46     known Q4P1 (4-node quadrilateral displacement element with 1-node piecewise

constant pressure element) and Q8P3. Globally, using continuous shape functions to link the local pressure DOFs in each element can also reduce the total number of pressure DOFs and increase the constraint ratio, such as with T6P3 (6-node triangular displacement element with 3-node continuous linear pressure element) and Q9P4 (Taylor–Hood element) [9]. These schemes belong to the mixed formulation framework and can also be implemented through a projection approach, where the pressure approximant is projected into a lower-dimensional space. Examples include selective integration methods [10, 11], B–bar or F–bar methods [12, 13, 14, 15, 16], pressure projection methods [17, 18], and the enhanced strain method [19]. Meanwhile, conventional 3-node triangular elements arranged in a regular cross pattern can also reduce the dimension of the pressure space [20]. It should be noted that not all of these methods can meet the inf–sup condition despite alleviating volumetric locking and producing a good displacement solution. Some methods, like Q4P1, show significant oscillation for the pressure solution, known as spurious pressure mode or checkerboard mode [20]. In such cases, additional stabilization approaches, such as multi-scale stabilization (VMS) [21, 22, 23, 24] or Galerkin/least-squares (GLS) [25], are required to eliminate the oscillations in pressure.

Another class of FEM methods adjusts the constraint ratio by increasing the displacement DOFs. For instance, based on 3-node triangular elements, Arnold et al. used a cubic bubble function in each element to increase the displacement DOFs, known as the MINI element [26, 27]. It has been shown that this method belongs to the VMS framework [28], and its fulfillment of the inf–sup condition can be analytically evidenced using the two-level projection framework [7]. The Crouzeix–Raviart element [29] transfers the DOFs from the triangular vertices to edges, increasing the constraint ratio since, for triangular topology, the number of edges is greater than that of vertices. More details about FEM technology for divergence constraint issues can be found in Refs. [2, 4, 30].

In the past two decades, various novel approximations equipped with global smoothed shape functions, such as moving least-squares approximation [31], reproducing kernel approximation [32], radial basis functions [33, 34], maximum-entropy approximation [35], and NURBS approximation [36, 37], have been proposed. In these approaches, the approximant pressure evaluated by the derivatives of global continuous shape functions also maintains a constraint ratio of 2 in 2D incompressible elasticity problems. However, the corresponding results still show lower accuracy caused by locking [38, 39]. Widely-used locking-free technologies for FEM are introduced in these approaches to enhance their performance. For example, Moutsanidis et al. employed selective integration and B–bar, F–bar methods for reproducing kernel particle methods [40, 41]. Wang et al. applied selective integration schemes with bubble–stabilized functions to node–based smoothed particle FEM [42]. Elguedj et al. proposed the B–bar and F–bar NURBS formulations for linear and nonlinear incompressible elasticity. Chen et al. adopted the pressure projection approach for reproducing kernel formulations for nearly–incompressible problems [43], which was later extended to Stokes flow formulations by Goh et al. [44]. Bombarde et al. developed a block–wise NURBS formulation for shell structures, eliminating locking via

93 pressure projection [45]. Most of these approximations offer better flexibility for  
94 arranging DOFs since their shape function constructions are no longer element-  
95 dependent. Huerta et al. proposed a reproducing kernel approximation with  
96 divergence-free basis functions to avoid volumetric strain entirely [46], although  
97 this approach is unsuitable for compressible cases. Wu et al. added extra dis-  
98 placement DOFs in FEM elements to resolve the locking issue, constructing  
99 local shape functions using generalized meshfree interpolation to maintain con-  
100istency [47]. Vu-Huu et al. employed different-order polygonal finite element  
101 shape functions to approximate displacement and pressure, embedding a bubble  
102 function in each element for stabilization.

103 This work proposes a more precise optimal divergence constraint ratio and  
104 implements a locking-free mixed FEM-Meshfree formulation with this optimal  
105 constraint ratio. Firstly, the inf-sup condition is derived in a new form, showing  
106 that the inf-sup value equals the lowest non-zero eigenvalue of dilatation stiff-  
107 ness in the context of variational analysis. Subsequently, involving a complete  
108 polynomial space with dimensions identical to displacement DOFs, the num-  
109ber of non-zero eigenvalues can be analytically calculated, and a new estimator  
110 considering the constraint ratio is established. From this estimator, the opti-  
111 mal constraint ratio is defined with a stabilized number of pressure nodes. If  
112 the constraint ratio exceeds the locking ratio, the formulation will show severe  
113 locking. When the constraint ratio is lower than the optimal ratio, the formu-  
114lation achieves satisfactory results, and the inf-sup condition is fulfilled. This  
115 estimator provides a strong link between the inf-sup value and the pressure  
116 DOFs, making it possible to justify the locking status by counting the pressure  
117 nodes. Furthermore, a mixed FEM-Meshfree formulation is proposed to verify  
118 the optimal constraint ratio. In this mixed formulation, the displacement is  
119 approximated by traditional finite element methods, and the pressure is dis-  
120cretized by reproducing kernel meshfree approximation. With the aid of global  
121 RK shape functions, the pressure's DOFs can be adjusted arbitrarily without  
122 considering approximation order and numerical integration issues to maintain-  
123 ing the constraint ratio as optimal.

124 The remainder of this paper is organized as follows: Section 2 reviews the  
125 mixed-formulation framework for incompressible elasticity problems. In Section  
126 3, a novel estimator of the inf-sup value is developed, from which the optimal  
127 constraint ratio is obtained. Section 4 introduces the mixed FEM-Meshfree  
128 formulation and its corresponding nodal distribution schemes. Section 5 verifies  
129 the proposed optimal constraint ratio using a set of benchmark incompressible  
130 elasticity examples, studying error convergence and stability properties for the  
131 mixed FEM-Meshfree approximation. Finally, the conclusions are presented in  
132 Section 6.

## 133 2. Mixed-formulation

### 134 2.1. Nearly-incompressible elasticity

135 Consider a body  $\Omega \in \mathbb{R}^{n_d}$  with boundary  $\Gamma$  in  $n_d$ -dimension, where  $\Gamma_t$  and  
136  $\Gamma_g$  denote its natural boundary and essential boundary, respectively, such that

<sup>137</sup>  $\Gamma_t \cup \Gamma_g = \Gamma$ ,  $\Gamma_t \cap \Gamma_g = \emptyset$ . The corresponding governing equations for the  
<sup>138</sup> mixed-formulation are given by:

$$\begin{cases} \nabla \cdot \boldsymbol{\sigma} + \mathbf{b} = \mathbf{0} & \text{in } \Omega \\ \frac{p}{\kappa} + \nabla \cdot \mathbf{u} = 0 & \text{in } \Omega \\ \boldsymbol{\sigma} \cdot \mathbf{n} = \mathbf{t} & \text{on } \Gamma_t \\ \mathbf{u} = \mathbf{g} & \text{on } \Gamma_g \end{cases} \quad (2)$$

<sup>139</sup> where  $\mathbf{u}$  and  $p$ , standing for displacement and hydrostatic pressure, respectively,  
<sup>140</sup> are the variables of this problem.  $\boldsymbol{\sigma}$  denotes the stress tensor and has the  
<sup>141</sup> following form:

$$\boldsymbol{\sigma}(\mathbf{u}, p) = p\mathbf{1} + 2\mu\nabla^d\mathbf{u} \quad (3)$$

<sup>142</sup> in which  $\mathbf{1} = \delta_{ij}\mathbf{e}_i \otimes \mathbf{e}_j$  is the second-order identity tensor.  $\nabla^d\mathbf{u}$  is the deviatoric  
<sup>143</sup> gradient of  $\mathbf{u}$  and can be evaluated by:

$$\nabla^d\mathbf{u} = \frac{1}{2}(\mathbf{u}\nabla + \nabla\mathbf{u}) - \frac{1}{3}\nabla \cdot \mathbf{u} \quad (4)$$

<sup>144</sup> and  $\kappa, \mu$  are the bulk modulus and shear modulus, respectively, and they can  
<sup>145</sup> be represented by Young's modulus  $E$  and Poisson's ratio  $\nu$ :

$$\kappa = \frac{E}{2(1-2\nu)}, \quad \mu = \frac{E}{2(1+\nu)} \quad (5)$$

<sup>146</sup> Moreover,  $\mathbf{b}$  denotes the prescribed body force in  $\Omega$ .  $\mathbf{t}, \mathbf{g}$  are prescribed  
<sup>147</sup> traction and displacement on natural and essential boundaries, respectively.

<sup>148</sup> In accordance with the Galerkin formulation, the weak form can be given  
<sup>149</sup> by: Find  $\mathbf{u} \in V, p \in Q$ ,

$$\begin{cases} a(\mathbf{v}, \mathbf{u}) + b(\mathbf{v}, p) = f(\mathbf{v}) & \forall \mathbf{v} \in V \\ b(\mathbf{u}, q) + c(q, p) = 0 & \forall q \in Q \end{cases} \quad (6)$$

<sup>150</sup> with the spaces  $V, Q$  defined by:

$$V = \{\mathbf{v} \in H^1(\Omega)^2 \mid \mathbf{v} = \mathbf{g}, \text{ on } \Gamma_g\} \quad (7)$$

$$Q = \{q \in L^2(\Omega) \mid \int_{\Omega} q d\Omega = 0\} \quad (8)$$

<sup>152</sup> where  $a : V \times V \rightarrow \mathbb{R}$ ,  $b : V \times Q \rightarrow \mathbb{R}$  and  $c : Q \times Q \rightarrow \mathbb{R}$  are bilinear forms,  
<sup>153</sup> and  $f : V \rightarrow \mathbb{R}$  is the linear form. In elasticity problems, they are given by:

$$a(\mathbf{v}, \mathbf{u}) = \int_{\Omega} \nabla^d\mathbf{v} : \nabla^d\mathbf{u} d\Omega \quad (9)$$

$$b(\mathbf{v}, q) = \int_{\Omega} \nabla \cdot \mathbf{v} q d\Omega \quad (10)$$

$$c(q, p) = - \int_{\Omega} \frac{1}{3\kappa} q p d\Omega \quad (11)$$

$$f(\mathbf{v}) = \int_{\Gamma_t} \mathbf{v} \cdot \mathbf{t} d\Gamma + \int_{\Omega} \mathbf{v} \cdot \mathbf{b} d\Omega \quad (12)$$

154      *2.2. Ritz–Galerkin problem and volumetric locking*

155      In the mixed-formulation framework, the displacement and pressure can be  
 156      discretized by different approximations. The approximant displacement  $\mathbf{u}_h$  and  
 157      approximant pressure  $p_h$  can be expressed by:

$$\mathbf{u}_h(\mathbf{x}) = \sum_{I=1}^{n_u} N_I(\mathbf{x}) \mathbf{u}_I, \quad p_h(\mathbf{x}) = \sum_{K=1}^{n_p} \Psi_K(\mathbf{x}) p_K \quad (13)$$

158      leading these approximations into the weak form of Eq. (6) yields the following  
 159      Ritz–Galerkin problems: Find  $\mathbf{u}_h \in V_h$ ,  $p_h \in Q_h$ ,

$$\begin{cases} a(\mathbf{v}_h, \mathbf{u}_h) + b(\mathbf{v}_h, p_h) = f(\mathbf{v}_h) & \forall \mathbf{v}_h \in V_h \\ b(\mathbf{u}_h, q_h) + c(q_h, p_h) = 0 & \forall q_h \in Q_h \end{cases} \quad (14)$$

160      For nearly incompressible material, the Poisson ratio approaches 0.5, and  
 161      the bulk modulus  $\kappa$  will tend to infinity based on Eq. (5). Then, the bilinear  
 162      form  $c$  in Eq. (11) tends to zero. And the weak form of Eq. (14) becomes an  
 163      enforcement of the volumetric strain  $\nabla \cdot \mathbf{u}_h$  to be zero using the Lagrangian  
 164      multiplier method, where  $p_h$  is the Lagrangian multiplier.

165      Furthermore, from the second line of Eq. (14), we have:

$$b(\mathbf{u}_h, q_h) + c(q_h, p_h) = (q_h, \nabla \cdot \mathbf{u}_h) - (q_h, \frac{1}{3\kappa} p_h) = 0, \quad \forall q_h \in Q_h \quad (15)$$

166      or

$$(q_h, 3\kappa \nabla \cdot \mathbf{u}_h - p_h) = 0, \quad \forall q_h \in Q_h \quad (16)$$

167      where  $(\bullet, \bullet)$  is the inner product operator evaluated by:

$$(q, p) := \int_{\Omega} q p d\Omega \quad (17)$$

168      Obviously, in Eq. (16),  $p_h$  is the orthogonal projection of  $3\kappa \nabla \cdot \mathbf{u}_h$  with respect  
 169      to the space  $Q_h$  [1], and, for further development, we use the nabla notation  
 170      with an upper tilde to denote the projection operator, i.e.,  $p_h = \tilde{\nabla} \cdot \mathbf{u}_h$ . In this  
 171      circumstance, the bilinear form  $b$  in the first line of Eq. (14) becomes:

$$\begin{aligned} b(\mathbf{v}_h, p_h) &= (\nabla \cdot \mathbf{v}_h - \tilde{\nabla} \cdot \mathbf{v}_h, p_h) + (\tilde{\nabla} \cdot \mathbf{v}_h, p_h) \\ &= (\tilde{\nabla} \cdot \mathbf{v}_h, 3\kappa \tilde{\nabla} \cdot \mathbf{u}_h) \\ &= \tilde{a}(\mathbf{v}_h, \mathbf{u}_h) \end{aligned} \quad (18)$$

172      where the bilinear form  $\tilde{a} : V_h \times V_h \rightarrow \mathbb{R}$  is defined by:

$$\tilde{a}(\mathbf{v}_h, \mathbf{u}_h) = \int_{\Omega} 3\kappa \tilde{\nabla} \cdot \mathbf{v}_h \tilde{\nabla} \cdot \mathbf{u}_h d\Omega \quad (19)$$

173      Accordingly, the problem of Eq. (14) becomes a one-variable form: Find  
 174       $\mathbf{u}_h \in V_h$ ,

$$a(\mathbf{v}_h, \mathbf{u}_h) + \tilde{a}(\mathbf{v}_h, \mathbf{u}_h) = f(\mathbf{v}_h), \quad \forall \mathbf{v}_h \in V_h \quad (20)$$

175 As  $\kappa \rightarrow \infty$ , Eq. (20) can be regarded as an enforcement of volumetric strain  
 176 using the penalty method, where  $\tilde{a}$  is the penalty term. However, it should  
 177 be noted that, if the mixed-formulation wants to obtain a satisfactory result,  
 178 this orthogonal projection must be surjective [48]. In the case where it is not  
 179 surjective, for a given  $p_h \in Q_h$ , it may not be possible to find a  $\mathbf{u}_h \in V_h$  such that  
 180  $p_h = 3\kappa \nabla \cdot \mathbf{u}_h$ . This will lead to a much smaller displacement than expected and  
 181 an oscillated pressure result. This phenomenon is called volumetric locking.

### 182 3. Optimal volumetric constraint ratio

#### 183 3.1. Inf-sup condition and its eigenvalue problem

184 To ensure the surjectivity of orthogonal projection and satisfactory results,  
 185 the approximations of Eq.(7) should satisfy the inf-sup condition, also known  
 186 as the Ladyzhenskaya–Babuška–Brezzi condition [4]:

$$\inf_{q_h \in Q_h} \sup_{\mathbf{v}_h \in V_h} \frac{|b(q_h, \mathbf{v}_h)|}{\|q_h\|_Q \|\mathbf{v}_h\|_V} \geq \beta > 0 \quad (21)$$

187 in which  $\beta$ , namely the inf-sup value, is a constant independent of the char-  
 188 acterized element size  $h$ . The norms  $\|\bullet\|_V$  and  $\|\bullet\|_Q$  can be flexibly defined  
 189 by:

$$\|\mathbf{v}\|_V^2 := \int_{\Omega} \nabla^d \mathbf{v} : \nabla^d \mathbf{v} d\Omega \quad (22)$$

$$\|q\|_Q^2 := \int_{\Omega} \frac{1}{3\kappa} q^2 d\Omega \quad (23)$$

190 To establish the relationship between the inf-sup condition and the con-  
 191 straint ratio, the inf-sup condition is firstly transformed by the following Lemma  
 192 1:

193 **Lemma 1.** Suppose  $\mathcal{P}_h : V_h \rightarrow Q_h$  is the orthogonal projection operator of the  
 194 divergence operator  $\mathcal{P} := 3\kappa \nabla \cdot$ , i.e.,  $\mathcal{P}_h := 3\kappa \tilde{\nabla} \cdot$  and satisfies Eq. (16). Then,  
 195 the inf-sup value can be estimated by:

$$\beta \leq \inf_{V'_h \subset V_h \setminus \ker \mathcal{P}_h} \sup_{\mathbf{v}_h \in V'_h} \frac{\|\mathcal{P}_h \mathbf{v}_h\|_Q}{\|\mathbf{v}_h\|_V} \quad (24)$$

196 in which  $\ker \mathcal{P}_h \subset V$  is the kernel of  $\mathcal{P}_h$  defined by  $\ker \mathcal{P}_h := \{\mathbf{v} \in V \mid \mathcal{P}_h \mathbf{v} = 0\}$ .

197 PROOF. As the definition of  $\mathcal{P}_h$ ,  $\text{Im} \mathcal{P}_h \subset Q_h$ , Eq. (21) can be rewritten as:

$$\begin{aligned} \beta &\leq \inf_{q_h \in Q_h} \sup_{\mathbf{v}_h \in V_h} \frac{|b(q_h, \mathbf{v}_h)|}{\|q_h\|_Q \|\mathbf{v}_h\|_V} = \inf_{q_h \in Q_h} \sup_{\mathbf{v}_h \in V_h} \frac{|(q_h, \frac{1}{3\kappa} \mathcal{P} \mathbf{v}_h)|}{\|q_h\|_Q \|\mathbf{v}_h\|_V} \\ &\leq \inf_{q_h \in \text{Im} \mathcal{P}_h} \sup_{\mathbf{v}_h \in V_h} \frac{|\frac{1}{3\kappa} (q_h, \mathcal{P}_h \mathbf{v}_h)|}{\|q_h\|_Q \|\mathbf{v}_h\|_V} \end{aligned} \quad (25)$$

<sup>198</sup> For a given  $q_h \in \text{Im}\mathcal{P}_h$ , suppose a space  $V'_h \subseteq V_h \setminus \ker \mathcal{P}_h$  defined by:

$$V'_h = \{\mathbf{v}_h \in V_h \mid \mathcal{P}_h \mathbf{v}_h = q_h\} \quad (26)$$

<sup>199</sup> Since  $\text{Im}\mathcal{P}_h \subset Q_h$ , according to the Cauchy-Schwarz inequality, we have:

$$\left| \frac{1}{3\kappa} (q_h, \mathcal{P}_h \mathbf{v}_h) \right| \leq \|q_h\|_Q \|\mathcal{P}_h \mathbf{v}_h\|_Q \quad (27)$$

<sup>200</sup> where this equality holds if and only if  $q_h = \mathcal{P}_h \mathbf{v}_h$ , i.e.,

$$\left| \frac{1}{3\kappa} (q_h, \mathcal{P}_h \mathbf{v}_h) \right| = \|q_h\|_Q \|\mathcal{P}_h \mathbf{v}_h\|_Q, \quad \forall \mathbf{v}_h \in V'_h \quad (28)$$

<sup>201</sup> And the following relationship can be evidenced:

$$\sup_{\mathbf{v}_h \in V_h} \frac{\left| \frac{1}{3\kappa} (q_h, \mathcal{P}_h \mathbf{v}_h) \right|}{\|q_h\|_Q \|\mathbf{v}_h\|_V} = \sup_{\mathbf{v}_h \in V'_h} \frac{\|\mathcal{P}_h \mathbf{v}_h\|_Q}{\|\mathbf{v}_h\|_V}, \quad \forall q_h \in \text{Im}\mathcal{P}_h \quad (29)$$

<sup>202</sup> Consequently, with a combination of Eqs. (25) and (29), Eq. (24) can be  
<sup>203</sup> obtained.

<sup>204</sup> **Remark 1.** With Lemma 1 and the norm definitions in Eqs. (22),(23), the  
<sup>205</sup> square of the inf-sup value can further be bounded by:

$$\beta^2 \leq \inf_{V'_h \subset V_h \setminus \ker \mathcal{P}_h} \sup_{\mathbf{v}_h \in V'_h} \frac{\|\mathcal{P}_h \mathbf{v}_h\|_Q^2}{\|\mathbf{v}_h\|_V^2} = \inf_{V'_h \subset V_h \setminus \ker \mathcal{P}_h} \sup_{\mathbf{v}_h \in V'_h} \frac{\tilde{a}(\mathbf{v}_h, \mathbf{v}_h)}{a(\mathbf{v}_h, \mathbf{v}_h)} \quad (30)$$

<sup>206</sup> The left-hand side of the above equation is consistent with the minimum-maximum  
<sup>207</sup> principle [49] and again proves the equivalence with the traditional numerical  
<sup>208</sup> inf-sup test [5]. Since that,  $\beta^2$  evaluates the non-zero general eigenvalue of  $\tilde{a}$   
<sup>209</sup> and  $a$  in Eq. (20).

### <sup>210</sup> 3.2. Inf-sup value estimator

<sup>211</sup> **Theorem 1.** Suppose that  $P_{n_u}$  is a polynomial space with  $n_u$  dimensions, and  
<sup>212</sup>  $V_{n_u}$  is the polynomial displacement space,  $V_{n_u} = P_{n_u}^{n_d}$ . The inf-sup value  $\beta$  can  
<sup>213</sup> further be bounded by:

$$\beta \leq \beta_s + Ch \quad (31)$$

<sup>214</sup> with

$$\beta_s = \inf_{V' \subset V_{n_u} \setminus \ker \mathcal{P}_h \mathcal{I}_h} \sup_{\mathbf{v} \in V'} \frac{\|\mathcal{P}\mathbf{v}\|_Q}{\|\mathbf{v}\|_V} \quad (32)$$

<sup>215</sup> where  $\mathcal{I}_h$  is the interpolation operator of the finite element approximation, and  
<sup>216</sup> correspondingly,  $h$  is the characterized distance between control nodes.

<sup>217</sup> PROOF. As the dimensions of  $V_h$  and  $V_{n_u}$  are identical,  $\dim V_{n_u} = \dim V_h =$   
<sup>218</sup>  $n_d \times n_u$ . There exists a unique  $\mathbf{v} \in V_{n_u}$  satisfying  $\mathbf{v}_h = \mathcal{I}_h \mathbf{v}$ . And the right side  
<sup>219</sup> of Eq. (24) becomes:

$$\inf_{V'_h \subset V_h \setminus \ker \mathcal{P}_h} \sup_{\mathbf{v}_h \in V'_h} \frac{\|\mathcal{P}_h \mathbf{v}_h\|_Q}{\|\mathbf{v}_h\|_V} = \inf_{V' \subset V_{n_u} \setminus \ker \mathcal{P}_h \mathcal{I}_h} \sup_{\mathbf{v} \in V'} \frac{\|\mathcal{P}_h \mathcal{I}_h \mathbf{v}\|_Q}{\|\mathcal{I}_h \mathbf{v}\|_V} \quad (33)$$

<sup>220</sup> According to the triangular inequality, Cauchy-Schwarz inequality, and the  
<sup>221</sup> relationship of Eqs. (16), we have:

$$\begin{aligned} \|\mathcal{P}_h \mathcal{I}_h \mathbf{v}\|_Q &= \sup_{q_h \in Q_h} \frac{|\frac{1}{3\kappa}(q_h, \mathcal{P}_h \mathcal{I}_h \mathbf{v})|}{\|q_h\|_Q} = \sup_{q_h \in Q_h} \frac{|(q_h, \mathcal{P} \mathcal{I}_h \mathbf{v})|}{\|q_h\|_Q} \\ &\leq \sup_{q_h \in Q_h} \frac{|(q_h, \mathcal{P} \mathbf{v})| + |(q_h, \mathcal{P} \mathbf{v} - \mathcal{P} \mathcal{I}_h \mathbf{v})|}{\|q_h\|_Q} \quad (34) \\ &\leq \|\mathcal{P} \mathbf{v}\|_Q + \|\mathcal{P}(\mathcal{I} - \mathcal{I}_h)\mathbf{v}\|_Q \end{aligned}$$

<sup>222</sup> Obviously, the second term on the right side of Eq. (34) is the interpolation  
<sup>223</sup> error, and can be evaluated by [50]:

$$\|\mathcal{P}(\mathcal{I} - \mathcal{I}_h)\mathbf{v}\|_Q \leq Ch \|\mathbf{v}\|_V \quad (35)$$

<sup>224</sup> Further leading the relation  $\|\mathcal{I}_h \mathbf{v}\|_V \geq C \|\mathbf{v}\|_V$  obtained from the closed  
<sup>225</sup> graph theorem [28] and considering Eqs. (34)-(35), the right-hand side of Eq.  
<sup>226</sup> (33) can be represented as:

$$\inf_{V' \subset V_{n_u} \setminus \ker \mathcal{P}_h \mathcal{I}_h} \sup_{\mathbf{v} \in V'} \frac{\|\mathcal{P}_h \mathcal{I}_h \mathbf{v}\|_Q}{\|\mathcal{I}_h \mathbf{v}\|_V} \leq \inf_{V' \subset V_{n_u} \setminus \ker \mathcal{P}_h \mathcal{I}_h} \sup_{\mathbf{v} \in V'} \frac{\|\mathcal{P} \mathbf{v}\|_Q}{\|\mathbf{v}\|_V} + Ch \quad (36)$$

<sup>227</sup> Substituting Eqs. (33),(36) into (24) can finally prove Eqs. (31), (32).

<sup>228</sup> As we can see in Eqs. (31) and (32),  $\beta_s \geq 0$ , the  $\beta_s$  being equal to 0 or not  
<sup>229</sup> determines whether the formulation can satisfy the inf-sup condition. If  $\beta_s > 0$ ,  
<sup>230</sup> as the mesh refines, the second term on the right-hand side of Eq. (31) will  
<sup>231</sup> sharply reduce and can be ignored. In contrast, if  $\beta_s = 0$ , the second term will  
<sup>232</sup> dominate, and the inf-sup condition will not be satisfied, leading to numerical  
<sup>233</sup> instability.

### <sup>234</sup> 3.3. Polynomial-wise constraint counting

<sup>235</sup> From the above subsection, we can know that whether  $\beta_s$  is zero or not  
<sup>236</sup> determines whether the mixed-formulation can fulfill the inf-sup condition. Ac-  
<sup>237</sup> cording to the expression of  $\beta_s$  in Eq. (32), as  $\beta_s = 0$ , the variable  $\mathbf{v}$  should  
<sup>238</sup> belong to  $\ker \mathcal{P}$ , so the dimensions of the subspace in which  $\beta_s \neq 0$ , namely  $n_s$ ,  
<sup>239</sup> can be evaluated by:

$$n_s = \dim(V_{n_u} \setminus \ker \mathcal{P}) \quad (37)$$

<sup>240</sup> To further construct the relationship between the inf-sup value estimator in  
<sup>241</sup> Eq. (31) and the constraint ratio  $r = \frac{n_d \times n_u}{n_p}$ , we should find the displacement

<sup>242</sup> and pressure DOFs in Eq. (31). With the definition of  $V_{n_u}$ , the number of  
<sup>243</sup> displacement DOFs is easy to be evaluated by:

$$n_u = \dim V_{n_u} \quad (38)$$

<sup>244</sup> With well-posed nodal distributions of displacement and pressure, the number  
<sup>245</sup> of pressure DOFs has the following relationship:

$$n_p = \dim Q_h = \dim(\text{Im} \mathcal{P}_h) = \dim(V_{n_u} \setminus \ker \mathcal{P}_h \mathcal{I}_h) \quad (39)$$

<sup>246</sup> Fig. 1 illustrates how the relationship between  $n_s$ ,  $n_p$ , and  $n_u$  influences the  
<sup>247</sup> fulfillment of the inf-sup condition:

- <sup>248</sup> As  $n_p > n_s$ , there must exist a subspace in space  $V_{n_u} \setminus \ker \mathcal{P}_h \mathcal{I}_h$  belonging  
<sup>249</sup> to  $\ker \mathcal{P}$ , resulting in  $\beta_s = 0$ , i.e.,  $V_{n_u} \setminus \ker \mathcal{P}_h \mathcal{I}_h \cap \ker \mathcal{P} \neq \emptyset$ . At this cir-  
<sup>250</sup> cumstance, the inf-sup condition cannot be satisfied, and the formulation  
<sup>251</sup> will suffer from volumetric locking.
- <sup>252</sup> As  $n_p \leq n_s$ , for well-posed nodal distributions, the space  $V_{n_u} \setminus \ker \mathcal{P}_h \mathcal{I}_h$   
<sup>253</sup> may be a subset of  $V_{n_u} \setminus \ker \mathcal{P}$ . Then,  $\beta_s$  will remain nonzero, and the  
<sup>254</sup> formulation will be locking-free.

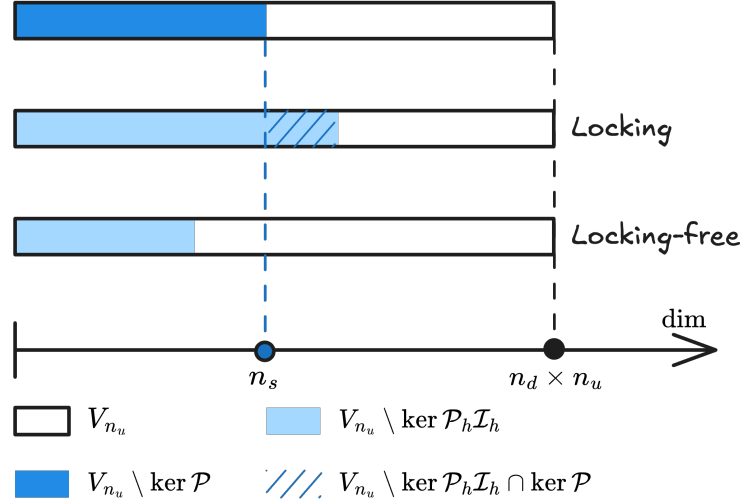


Figure 1: Illustration of estimator

<sup>255</sup> Summarily, the formulation can satisfy the inf-sup condition and alleviate  
<sup>256</sup> volumetric locking if at least the number of pressure nodes  $n_p$  is less than  $n_s$ ,  
<sup>257</sup> so we name  $n_s$  as the stabilized number of pressure nodes. At this moment,  
<sup>258</sup> the volumetric constraint ratio should meet the following relation to ensure the  
<sup>259</sup> inf-sup condition:

$$r_{opt} \geq \frac{n_d \times n_u}{n_s} \quad (40)$$

260 **Remark 2.** Some uniform elements with special arrangements, like the union-  
 261 jack element arrangement for 3-node triangular elements, can pass the inf-sup  
 262 test [6], but their pressure DOFs number is greater than  $n_s$ . This is because the  
 263 union-jack arrangement leads to a lower nonzero eigenvalue number of  $\tilde{a}$  and a  
 264 in Eq. (20), and the corresponding nonzero eigenvalue number is less than or  
 265 equal to the stabilized number  $n_s$ , satisfying Eq. (40). The similar cases about  
 266 this special element arrangement are too few, so it is more straightforward to  
 267 use the number of pressure nodes  $n_p$  to measure  $\dim(V_{n_u} \setminus \ker \mathcal{P}_h \mathcal{I}_h)$ .

268 **Remark 3.** It is obvious that the traditional optimal constraint ratio cannot  
 269 fulfill this condition. However, not all formulations satisfying this condition  
 270 can totally avoid volumetric locking. This is because  $n_p \leq n_s$  is not equivalent  
 271 to  $V_{n_u} \setminus \ker \mathcal{P}_h \mathcal{I}_h \subset V_{n_u} \setminus \ker \mathcal{P}$ . Fortunately, well-posed nodal distributions of  
 272 displacement and pressure can ensure this, which will be evidenced by numerical  
 273 examples in the subsequent sections.

274 *3.4. Optimal volumetric constraint ratio*

275 The fulfillment of the inf-sup condition should require the number of pres-  
 276 sure nodes  $n_p$  to be lower than the stabilized number  $n_s$ , and now, we will  
 277 demonstrate how to determine  $n_s$  for a specific number of displacement DOFs.

278 In the 2D case, for instance, we first consider the linear polynomial displace-  
 279 ment space  $V_3$  is given by:

$$V_3 = \text{span} \left\{ \begin{pmatrix} 1 \\ 0 \end{pmatrix}, \begin{pmatrix} 0 \\ 1 \end{pmatrix}, \begin{pmatrix} x \\ 0 \end{pmatrix}, \begin{pmatrix} 0 \\ x \end{pmatrix}, \begin{pmatrix} y \\ 0 \end{pmatrix}, \begin{pmatrix} 0 \\ y \end{pmatrix} \right\} \quad (41)$$

280 or rearranged as follows,

$$V_3 = \text{span} \left\{ \underbrace{\begin{pmatrix} 1 \\ 0 \end{pmatrix}, \begin{pmatrix} 0 \\ 1 \end{pmatrix}, \begin{pmatrix} y \\ 0 \end{pmatrix}, \begin{pmatrix} 0 \\ x \end{pmatrix}, \begin{pmatrix} x \\ -y \end{pmatrix}}_{\ker \mathcal{P}}, \underbrace{\begin{pmatrix} x \\ y \end{pmatrix}}_{V_3 \setminus \ker \mathcal{P}} \right\} \quad (42)$$

281 It can be counted that, for  $n_u = 3$ ,  $n_s = 1$ . Following the path, the displacement  
 282 space with a quadratic polynomial base, namely  $V_6$ , can be stated as:

$$V_6 = \text{span} \left\{ \underbrace{\begin{pmatrix} 1 \\ 0 \end{pmatrix}, \begin{pmatrix} 0 \\ 1 \end{pmatrix}, \begin{pmatrix} y \\ 0 \end{pmatrix}, \begin{pmatrix} 0 \\ x \end{pmatrix}, \begin{pmatrix} x \\ -y \end{pmatrix}, \begin{pmatrix} x^2 \\ -2xy \end{pmatrix}, \begin{pmatrix} y^2 \\ 0 \end{pmatrix}, \begin{pmatrix} 0 \\ x^2 \end{pmatrix}, \begin{pmatrix} -2xy \\ y^2 \end{pmatrix}}_{\ker \mathcal{P}}, \underbrace{\begin{pmatrix} x \\ y \end{pmatrix}, \begin{pmatrix} x^2 \\ 2xy \end{pmatrix}, \begin{pmatrix} 2xy \\ y^2 \end{pmatrix}}_{V_6 \setminus \ker \mathcal{P}} \right\} \quad (43)$$

283 In this circumstance,  $n_s = 3$ . As the order of the polynomial space increases, the  
 284 optimal numbers of constraint DOFs for each order of the polynomial space are  
 285 listed in Table. 1, in which  $n$  denotes the order of space  $P_{n_u}$ . For the flexibility  
 286 of usage, the relation between  $n_u$  and  $n_s$  is summarized as follows:

$$n_s = \frac{n(n+1)}{2}, \quad n = \left\lfloor \frac{\sqrt{1+8n_u} - 3}{2} \right\rfloor \quad (44)$$

Table 1: Relationship between displacement DOFs and stabilized number

n	2D		3D	
	$n_u$	$n_s$	$n_u$	$n_s$
1	3	1	4	1
2	6	3	10	4
3	10	6	20	10
4	15	10	35	20
$\vdots$	$\vdots$	$\vdots$	$\vdots$	$\vdots$

287 For the 3D case, following the path in 2D, the linear polynomial space  $V_4$  is  
288 considered herein, and the arranged space of  $V_4$  is listed as follows:

$$V_4 = \text{span} \left\{ \underbrace{\left( \begin{array}{c} 1 \\ 0 \\ 0 \end{array} \right), \left( \begin{array}{c} 0 \\ 1 \\ 0 \end{array} \right), \left( \begin{array}{c} 0 \\ 0 \\ 1 \end{array} \right), \left( \begin{array}{c} 0 \\ x \\ 0 \end{array} \right), \left( \begin{array}{c} 0 \\ 0 \\ x \end{array} \right), \left( \begin{array}{c} y \\ 0 \\ 0 \end{array} \right)}_{\ker \mathcal{P}}, \underbrace{\left( \begin{array}{c} 0 \\ y \\ 0 \end{array} \right), \left( \begin{array}{c} z \\ 0 \\ 0 \end{array} \right), \left( \begin{array}{c} 0 \\ z \\ 0 \end{array} \right), \left( \begin{array}{c} x \\ -y \\ 0 \end{array} \right), \left( \begin{array}{c} x \\ 0 \\ -z \end{array} \right), \left( \begin{array}{c} y \\ z \\ 0 \end{array} \right)}_{V_{n_u} \setminus \ker \mathcal{P}} \right\} \quad (45)$$

289 For brevity, the stabilized numbers for higher-order polynomial displacement  
290 spaces are directly listed in Table. 1, and it can be summarized that, for a given  
291 number of displacement DOFs, the stabilized number for pressure DOFs can be  
292 calculated as follows:

$$n_s = \frac{n(n+1)(n+2)}{6} \quad (46)$$

$$n = \left\lceil \left( 3n_u + \frac{1}{3}\sqrt{81n_u^2 - \frac{1}{3}} \right)^{\frac{1}{3}} + \frac{1}{3\left( 3n_u + \frac{1}{3}\sqrt{81n_u^2 - \frac{1}{3}} \right)^{\frac{1}{3}}} - 2 \right\rceil \quad (47)$$

293 Table 2 lists the effectiveness of the traditional constraint ratio and the  
294 proposed optimal constraint ratio for traditional mixed formulation schemes,  
295 comparing the constraint ratios with the fulfillment of the inf-sup condition  
296 using analytical proof and numerical prediction. The table reveals that the  
297 traditional constraint ratio  $r \geq n_d$  is not sufficient to guarantee the inf-sup  
298 condition, especially for low-order mixed formulations like T3P1 and Q4P1. The

299 proposed optimal constraint ratio  $r_{opt} \geq \frac{n_d \times n_u}{n_s}$  is more effective in ensuring the  
300 inf-sup condition.

Table 2: Constraint ratio and inf-sup condition for various mixed formulations

Formulation	Constraint Ratio $r \geq n_d$	Inf-sup condition Numerical prediction	Inf-sup condition Analytical proof	Constraint Ratio $r = r_{opt}$
T3P1( $r = 1$ )	✗	✗	✗	✗
Q4P1( $r = 2$ )	✓	✗	✗	✗
Q8P3( $r = 2$ )	✓	✗	✗	✗
Q8P1( $r = 6$ )	✓	✓	✓	✓
Q9P3( $r = \frac{8}{3}$ )	✓	✓	✓	✓
MINI( $r = \frac{8}{3}$ )	✓	✓	✓	✓
Taylor-Hood( $r = 8$ )	✓	✓	✓	✓
T6C3( $r = \frac{8}{3}$ )	✓	✓	✓	✓
Crouzeix-Raviart( $r = 4$ )	✓	✓	✓	✓

<sup>301</sup> **4. FE–Meshfree mixed formulation with optimal constraint**

<sup>302</sup> In the proposed mixed-formulation, the displacement is approximated using  
<sup>303</sup> three-node, six-node triangular elements and four-node, eight-node quadrilateral  
<sup>304</sup> elements [2]. In order to flexibly adjust to let the DOFs of pressure meet the  
<sup>305</sup> optimal constraint, the reproducing kernel meshfree approximation is involved  
<sup>306</sup> to approximate pressure.

<sup>307</sup> *4.1. Reproducing kernel meshfree approximation*

<sup>308</sup> In accordance with the reproducing kernel approximation, the entire domain  
<sup>309</sup>  $\Omega$  is discretized by  $n_p$  meshfree nodes,  $\{\mathbf{x}_I\}_{I=1}^{n_p}$ . The approximated pressure,  
<sup>310</sup> namely  $p_h$ , can be expressed by the shape function  $\Psi_I$  and nodal coefficient  $p_I$ ,  
<sup>311</sup> yields:

$$p_h(\mathbf{x}) = \sum_{I=1}^{n_p} \Psi_I(\mathbf{x}) p_I \quad (48)$$

<sup>312</sup> where, in the reproducing kernel approximation framework, the shape function  
<sup>313</sup>  $\Psi_I$  is given by:

$$\Psi_I(\mathbf{x}) = \mathbf{c}(\mathbf{x}_I - \mathbf{x}) \mathbf{p}(\mathbf{x}_I - \mathbf{x}) \phi(\mathbf{x}_I - \mathbf{x}) \quad (49)$$

<sup>314</sup> in which  $\mathbf{p}$  is the basis function, especially for the 2D quadratic basis function,  
<sup>315</sup> having the following form:

$$\mathbf{p}(\mathbf{x}) = \{1, x, y, x^2, xy, y^2\}^T \quad (50)$$

<sup>316</sup> and  $\phi$  stands for the kernel function. In this work, the traditional Cubic B–spline  
<sup>317</sup> function with square support is used as the kernel function:

$$\phi(\mathbf{x}_I - \mathbf{x}) = \phi(s_x) \phi(s_y), \quad s_i = \frac{\|\mathbf{x}_I - \mathbf{x}\|}{\bar{s}_{iI}} \quad (51)$$

<sup>318</sup> with

$$\phi(s) = \frac{1}{3!} \begin{cases} (2-2s)^3 - 4(1-2s)^3 & s \leq \frac{1}{2} \\ (2-2s)^3 & \frac{1}{2} < s < 1 \\ 0 & s > 1 \end{cases} \quad (52)$$

<sup>319</sup> where  $\bar{s}_{iI}$ 's are the support size towards the  $i$ -direction for the shape function  
<sup>320</sup>  $\Psi_I$ . The correction function  $\mathbf{c}$  can be determined by the following so-called  
<sup>321</sup> consistency condition:

$$\sum_{I=1}^{n_p} \Psi_I(\mathbf{x}) \mathbf{p}(\mathbf{x}_I) = \mathbf{p}(\mathbf{x}) \quad (53)$$

<sup>322</sup> or equivalent shifted form:

$$\sum_{I=1}^{n_p} \Psi_I(\mathbf{x}) \mathbf{p}(\mathbf{x}_I - \mathbf{x}) = \mathbf{p}(\mathbf{0}) \quad (54)$$

<sup>323</sup> Substituting Eq. 49 into Eq. (54) leads to:

$$\mathbf{c}(\mathbf{x}_I - \mathbf{x}) = \mathbf{A}^{-1}(\mathbf{x}_I - \mathbf{x})\mathbf{p}(\mathbf{0}) \quad (55)$$

<sup>324</sup> in which  $\mathbf{A}$  is namely the moment matrix evaluated by:

$$\mathbf{A}(\mathbf{x}_I - \mathbf{x}) = \sum_{I=1}^{n_p} \mathbf{p}(\mathbf{x}_I - \mathbf{x})\mathbf{p}^T(\mathbf{x}_I - \mathbf{x})\phi(\mathbf{x}_I - \mathbf{x}) \quad (56)$$

<sup>325</sup> Taking Eq. (55) back to Eq. (49), the final form of the reproducing kernel shape  
<sup>326</sup> function can be obtained as:

$$\Psi_I(\mathbf{x}) = \mathbf{p}^T(\mathbf{0})\mathbf{A}^{-1}(\mathbf{x}_I - \mathbf{x})\phi(\mathbf{x}_I - \mathbf{x}) \quad (57)$$

#### <sup>327</sup> 4.2. Optimal pressure nodes distributions

<sup>328</sup> In this subsection, the 2D and 3D inf-sup tests [6] with the FE-meshfree  
<sup>329</sup> mixed formulation are employed to validate the proposed estimator of the inf-  
<sup>330</sup> sup value. The 2D test considers the square domain  $\Omega = (0, 1) \otimes (0, 1)$  in Fig.  
<sup>331</sup> 3, where the displacement is discretized by linear Triangular element (Tri3),  
<sup>332</sup> Quadrilateral element (Quad4) with  $4 \times 4$ ,  $8 \times 8$ ,  $16 \times 16$  and  $32 \times 32$  elements,  
<sup>333</sup> quadratic Triangular element (Tri6), Quadrilateral element (Quad8) with  $2 \times 2$ ,  
<sup>334</sup>  $4 \times 4$ ,  $8 \times 8$  and  $16 \times 16$  elements, respectively. The 3D test employs a cube domain  
<sup>335</sup>  $\Omega = (0, 1) \otimes (0, 1) \otimes (0, 1)$  in Fig. 4 with  $4 \times 4$ ,  $8 \times 8$  and  $16 \times 16$  elements for the  
<sup>336</sup> 4-node tetrahedral element (Tet4) and 8-node hexahedral element (Hex8). In  
<sup>337</sup> order to avoid the influence of interpolation error, uniform nodal distributions  
<sup>338</sup> are used for pressure discretizations.

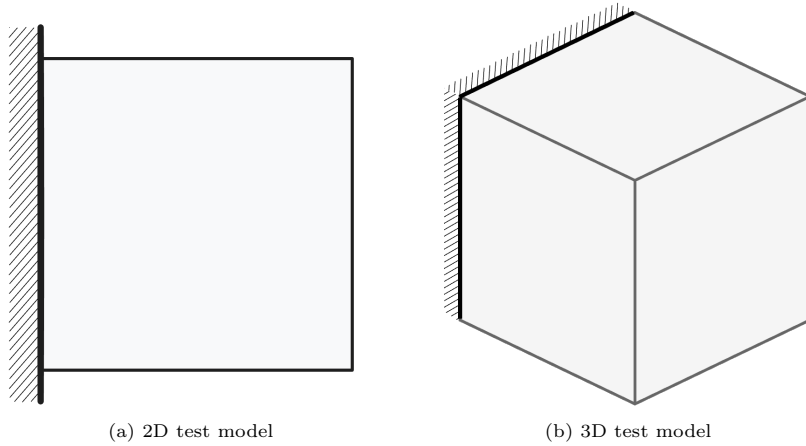


Figure 2: Illustration of inf-sup test

<sup>339</sup> Figures 3 and 4 show the corresponding results, in which the red line stands  
<sup>340</sup> for the value of  $\beta$  with respect to the number of pressure nodes  $n_p$ , and the

<sup>341</sup> vertical dashed line denotes the stabilized number  $n_s$ . The deeper color of  
<sup>342</sup> the lines means mesh refinement. The results show that, no matter linear or  
<sup>343</sup> quadratic elements, as  $n_p$  increases over  $n_s$ , the value of  $\beta$  sharply decreases,  
<sup>344</sup> and then the inf-sup condition cannot be maintained. This result is consistent  
<sup>345</sup> with the discussion in Section 3, and again verifies the effect of the proposed  
<sup>346</sup> estimator.

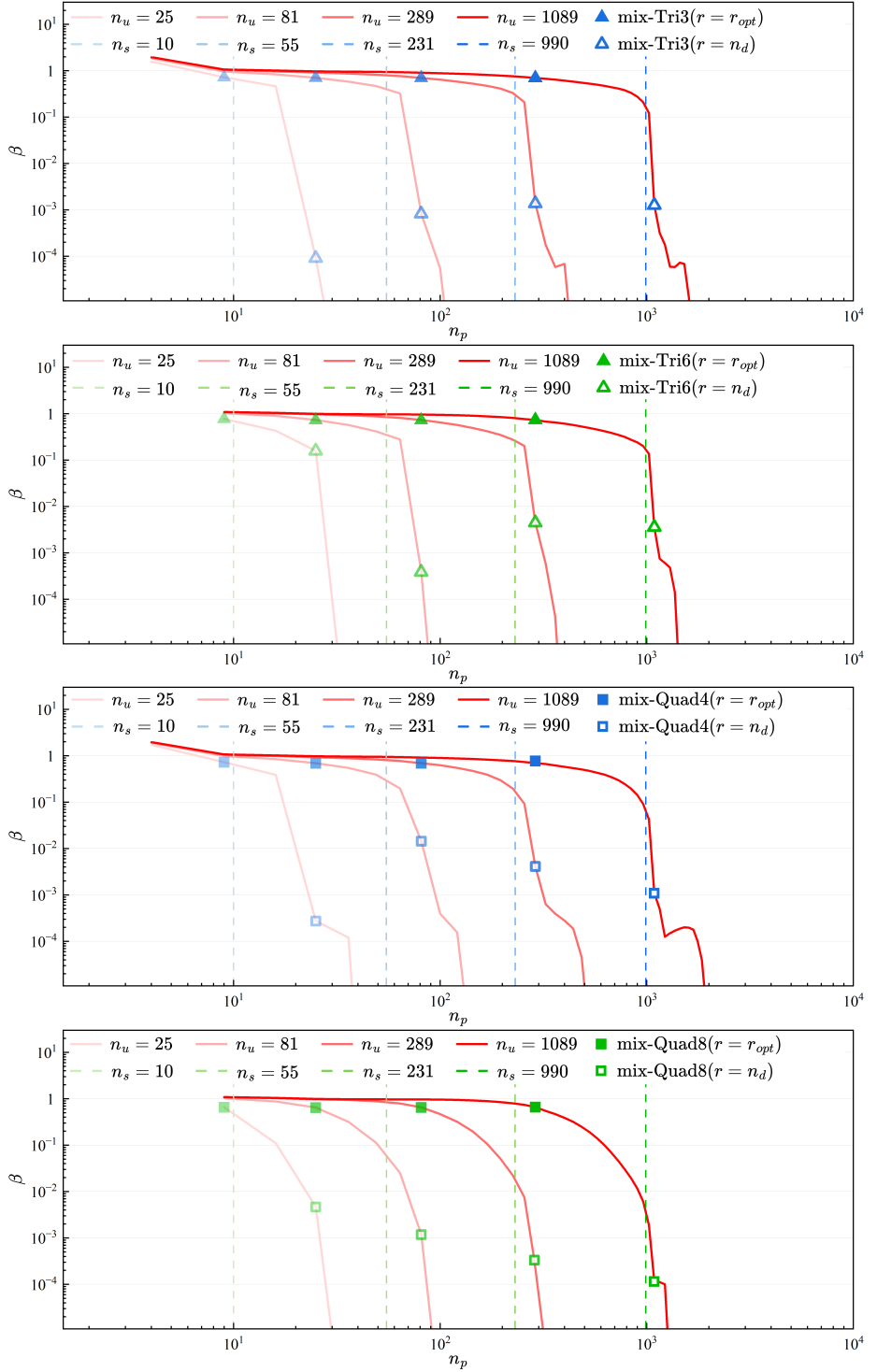


Figure 3: Inf-sup test for 2D mixed FE-meshfree formulations:  
(a) mix-Tri3; (b) mix-Tri6; (c) mix-Quad4; (d) mix-Quad8

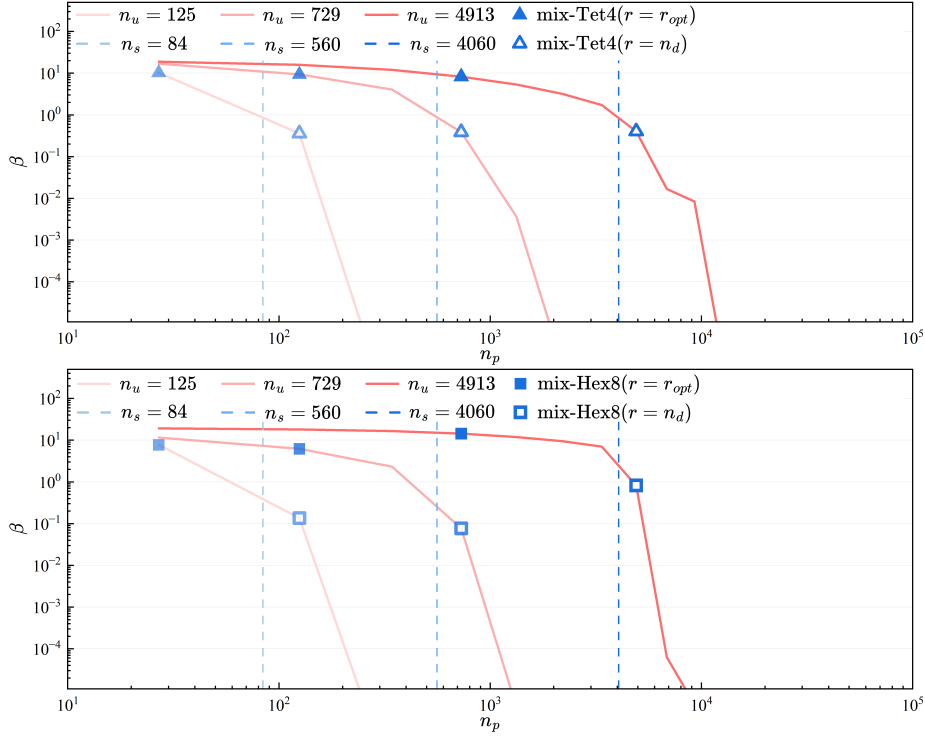


Figure 4: Inf-sup test for 3D mixed FE-meshfree formulations:  
 (a) mix-Tet4; (b) mix-Hex8

347 Moreover, the mixed formulation's results with the traditional optimal con-  
 348 straint ratio  $r = n_d$  are listed in 3 as well, and  $\beta$  in this circumstance is al-  
 349 ready much smaller than those in the optimal range. Considering the results  
 350 shown above, the easy programming and efficiency, the pressure nodes are cho-  
 351 sen among the displacement nodes. The final schemes for linear and quadratic,  
 352 2D and 3D element discretizations are shown in Figure 5, in which all constraint  
 353 ratios belong to the range of the optimal ratio. The corresponding inf-sup test  
 354 results for these schemes are also marked in Figure 2 and show that, with mesh  
 355 refinement, their  $\beta$ 's are always maintained at a non-negligible level.

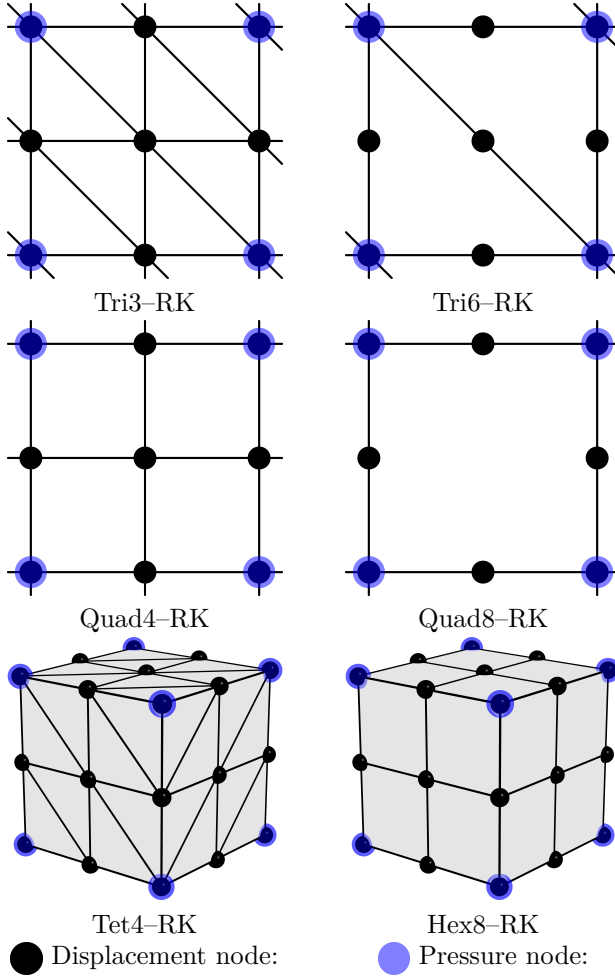


Figure 5: Nodal distribution schemes for FE-MF mixed formulations with  $r = r_{opt}$

356    **5. Numerical examples**

357    **5.1. Cantilever beam problem**

358    Consider the cantilever beam problem shown in Figure 6 with length  $L = 48$ ,  
 359    width  $D = 12$ , and the incompressible material parameters are employed with  
 360    Young's modulus  $E = 3 \times 10^6$ , Poisson's ratio  $\nu = 0.5 - 10^{-8}$ . The left hand  
 361    side is fixed and the right side subject to a concentrated force  $P = 1000$ . All  
 362    the prescribed values in the boundary conditions are evaluated by the analytical

<sup>363</sup> solution that is given as follows [51]:

$$\begin{cases} u_x(x) = -\frac{Py}{6EI} \left( (6L - 3x)x + (2 + \bar{\nu})(y^2 - \frac{D^2}{4}) \right) \\ u_y(x) = \frac{P}{6\bar{E}I} \left( 3\bar{\nu}y^2(L - x) + (4 + 5\bar{\nu})\frac{D^2x}{4} + (3L - x)x^2 \right) \end{cases} \quad (58)$$

<sup>364</sup> where  $I$  is the beam's moment of inertia,  $\bar{E}$  and  $\bar{\nu}$  are the material parameters  
<sup>365</sup> for plane strain hypothesis, they can be expressed by:

$$I = \frac{D^3}{12}, \quad \bar{E} = \frac{E}{1 - \nu^2}, \quad \bar{\nu} = \frac{\nu}{1 - \nu} \quad (59)$$

<sup>366</sup> And correspondingly, the stress components are evaluated by

$$\begin{cases} \sigma_{xx} = -\frac{P(L - x)y}{I} \\ \sigma_{yy} = 0 \\ \sigma_{xy} = \frac{P}{2I} \left( \frac{D^2}{4} - y^2 \right) \end{cases} \quad (60)$$

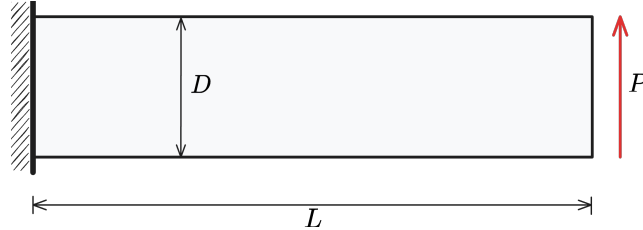


Figure 6: Illustration of cantilever beam problem

<sup>367</sup> In this problem, the Quad4 element with  $16 \times 4$ ,  $32 \times 8$ ,  $64 \times 16$ ,  $128 \times 32$   
<sup>368</sup> grids, and Quad8 element with  $8 \times 2$ ,  $16 \times 4$ ,  $32 \times 8$ ,  $64 \times 16$  grids are em-  
<sup>369</sup> ployed for displacement discretization. The pressure is discretized by linear and  
<sup>370</sup> quadratic meshfree approximations with 1.5 and 2.5 characterized support sizes  
<sup>371</sup> respectively. The strain and pressure errors with respect to pressure nodes  $n_p$   
<sup>372</sup> are displayed in Figure 7, where the vertical dashed lines stand for the stabi-  
<sup>373</sup> lized number  $n_s$ . The figure implies that the Quad8 shows better performance  
<sup>374</sup> than Quad4, since the Quad8's displacement results are stable no matter the  
<sup>375</sup> constraint ratio is in the optimal range or not. And the Quad4's displacement  
<sup>376</sup> errors increase as soon as  $n_p > n_s$ . However, both Quad4's and Quad8's pressure  
<sup>377</sup> errors immediately increase while their constraint ratios are out of the optimal  
<sup>378</sup> range, and Quad8 still has better results than Quad4. Figure 8 shows the strain  
<sup>379</sup> and pressure error convergence comparisons for this cantilever beam problem,  
<sup>380</sup> in which, except Quad8-RK( $r = 2$ ) for strain error, all formulations with the  
<sup>381</sup> traditional constraint ratio of  $r = 2$  cannot ensure the optimal error convergence

<sup>382</sup> rates. The proposed mixed formulations with  $r = r_{opt}$  can maintain the optimal  
<sup>383</sup> error convergence ratio and show better accuracy.

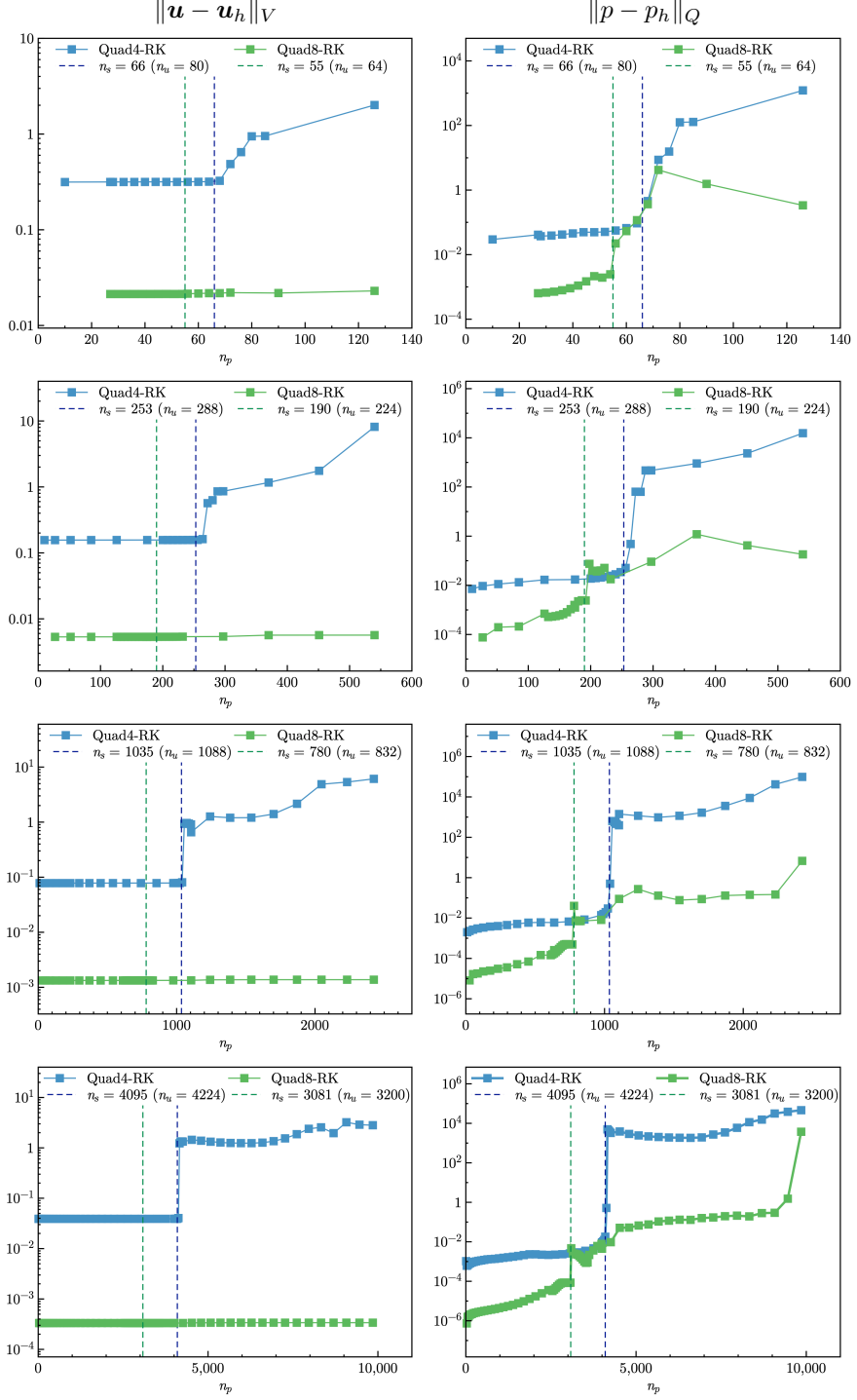


Figure 7: Strain and pressure errors vs.  $n_p$  for cantilever beam problem

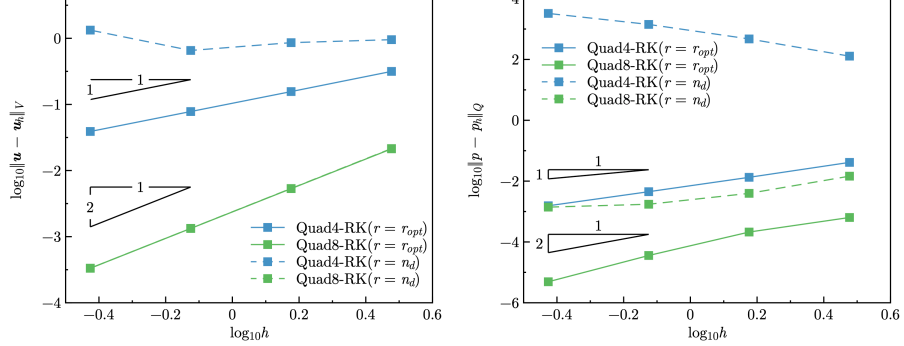


Figure 8: Error convergence study for cantilever beam problem: (a) Strain, (b) Pressure

### 384 5.2. Plate with hole problem

385 Consider an infinite plate with a hole centered at the origin, as shown in  
 386 Figure 9, and at the infinity towards the  $x$ -direction subjected to a uniform  
 387 traction  $T = 1000$ . The geometric and material parameters for this problem are  
 388 that the ratio of the hole  $a = 1$ , Young's modulus  $E = 3 \times 10^6$ , and Poisson's  
 389 ratio  $\nu = 0.5 - 10^{-8}$ . The analytical solution of this problem refers to the  
 390 Michell solution [51] as:

$$\begin{cases} u_x(\rho, \theta) = \frac{T a}{8\mu} \left( \frac{\rho}{a} (k+1) \cos \theta - \frac{2a^3}{\rho^3} \cos 3\theta + \frac{2a}{\rho} ((1+k) \cos \theta + \cos 3\theta) \right) \\ u_y(\rho, \theta) = \frac{T a}{8\mu} \left( \frac{\rho}{a} (k-3) \sin \theta - \frac{2a^3}{\rho^3} \sin 3\theta + \frac{2a}{\rho} ((1-k) \sin \theta + \sin 3\theta) \right) \end{cases} \quad (61)$$

391 in which  $k = \frac{3-\nu}{1+\nu}$ ,  $\mu = \frac{E}{2(1+\nu)}$ . And the stress components are given by:

$$\begin{cases} \sigma_{xx} = T \left( 1 - \frac{a^2}{\rho^2} \left( \frac{3}{2} \cos 2\theta + \cos 4\theta \right) + \frac{3a^4}{2\rho^4} \cos 4\theta \right) \\ \sigma_{yy} = -T \left( \frac{a^2}{\rho^2} \left( \frac{1}{2} \cos 2\theta - \cos 4\theta \right) + \frac{3a^4}{2\rho^4} \cos 4\theta \right) \\ \sigma_{xy} = -T \left( \frac{a^2}{\rho^2} \left( \frac{1}{2} \sin 2\theta + \sin 4\theta \right) - \frac{3a^4}{2\rho^4} \sin 4\theta \right) \end{cases} \quad (62)$$

392 According to the symmetry property of this problem, only a quarter model  
 393 with length  $b = 5$  is considered as shown in Figure 9. The displacement is  
 394 discretized by 3-node and 6-node triangular elements with 81, 299, 1089, and  
 395 4225 nodes. The corresponding linear and quadratic meshfree formulations are  
 396 employed for pressure discretization, and the characterized support sizes are  
 397 chosen as 1.5 and 2.5, respectively. Figure 10 studies the relationship between  
 398 strain, pressure errors, and  $n_p$ . Unlike the quadrilateral element case in Section  
 399 5.1, the quadratic Tri6–RK shows worse results while the constraint ratio is out  
 400 of the optimal range. And Tri3–RK exhibits less sensitivity in strain error than

401 Tri6–RK, but its error is increasing while  $n_p$  goes up. Both Tri3–RK and Tri6–  
 402 RK with constraint ratios under the optimal range perform acceptably. The  
 403 corresponding error convergence study is presented in Figure 11, and only Tri3–  
 404 RK with  $r = 2$  shows a comparable result with the optimal one with  $r = r_{opt}$ .  
 405 The other formulations with the traditional constraint ratio show lower accuracy  
 406 and error convergence rates.

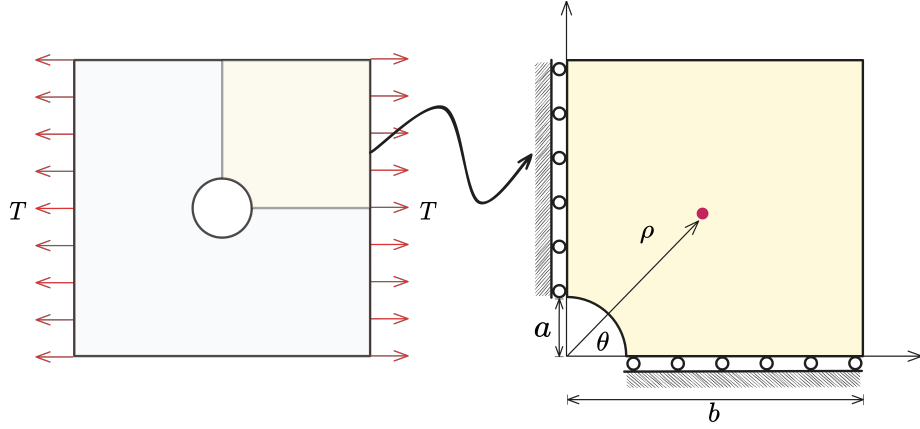


Figure 9: Illustration of plate with hole problem

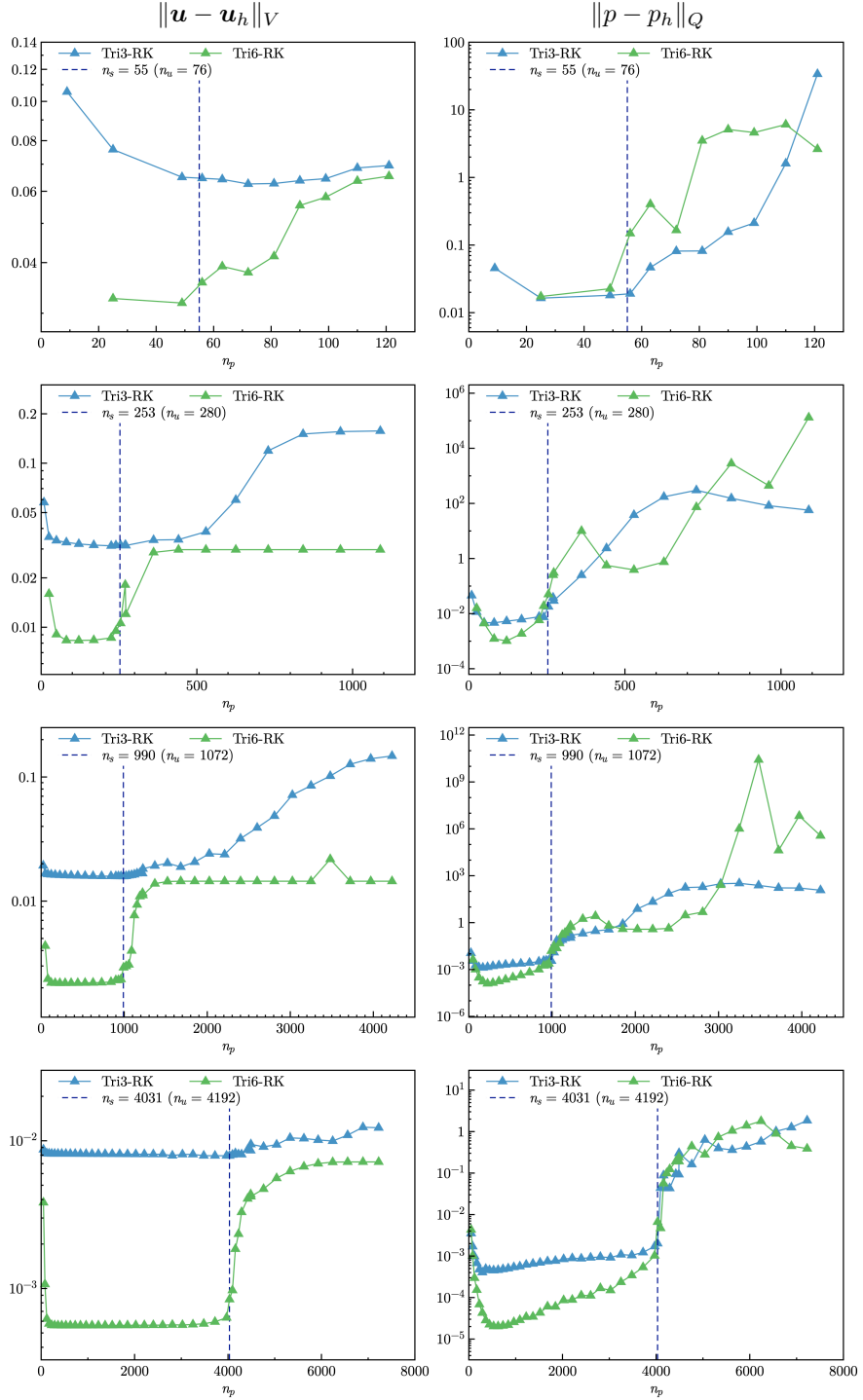


Figure 10: Strain and pressure errors vs.  $n_p$  for plate with hole problem

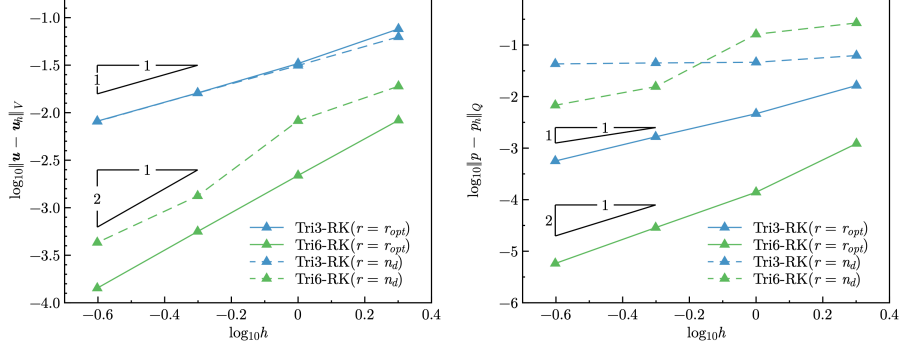


Figure 11: Error convergence study for plate with a hole problem: (a) Strain, (b) Pressure

407     5.3. Cook membrane problem

408     The Cook membrane problem [12] is used herein for stability analysis of  
409     pressure. The geometry of this problem is shown in Figure 12, in which the  
410     left hand side is fixed and the right hand side subjects a concentrated force  
411      $P = 1000$  in the  $y$ -direction. The material parameters are Young's modulus  
412      $E = 3 \times 10^6$  and Poisson's ratio  $\nu = 0.5 - 10^{-8}$ .

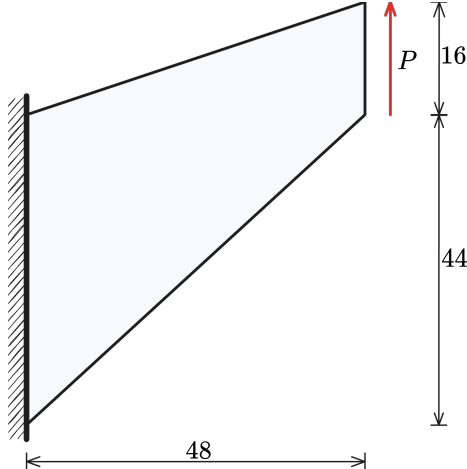


Figure 12: Illustration of Cook membrane problem

413     In this test, we focus on the pressure stability of 2D mixed FE-meshfree  
414     formulations. Figures 13–16 show the pressure contour plots for non-uniform  
415     Tri3-RK, Tri6-RK, Quad4-RK, and Quad8-RK formulations with  $r = n_d$  and  
416      $r = r_{opt}$ , respectively. The reproducing kernel meshfree approximations are  
417     employed for pressure discretization with characterized support sizes of 1.5 for  
418     the linear basis function and 2.5 for the quadratic basis function. The results  
419     imply that the pressure contour plots with the optimal constraint ratio  $r = r_{opt}$

<sup>420</sup> show a more stable and smooth pressure distribution compared to those with  
<sup>421</sup> the traditional constraint ratio  $r = n_d$ .

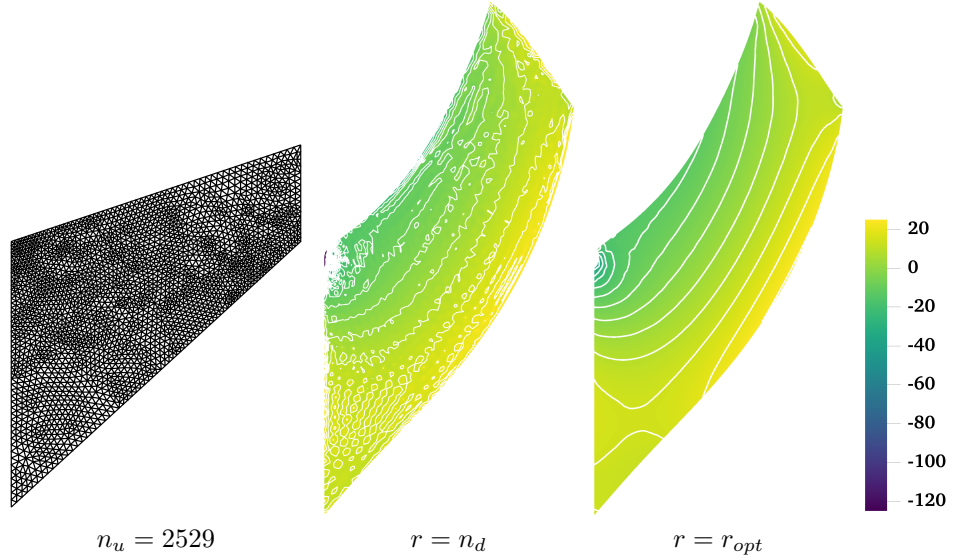


Figure 13: Comparison of pressure contour plots for Cook membrane problem with Tri3–RK

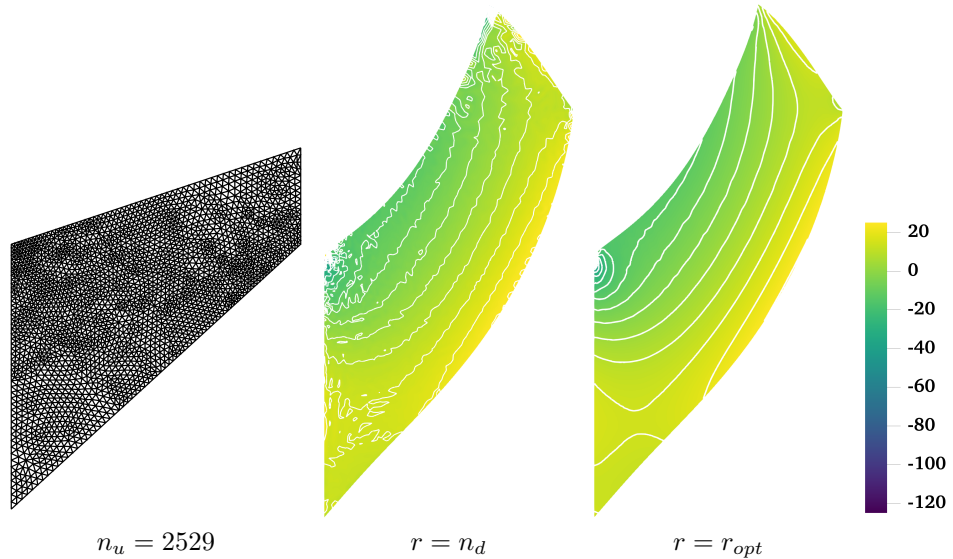


Figure 14: Comparison of pressure contour plots for Cook membrane problem with Tri6–RK

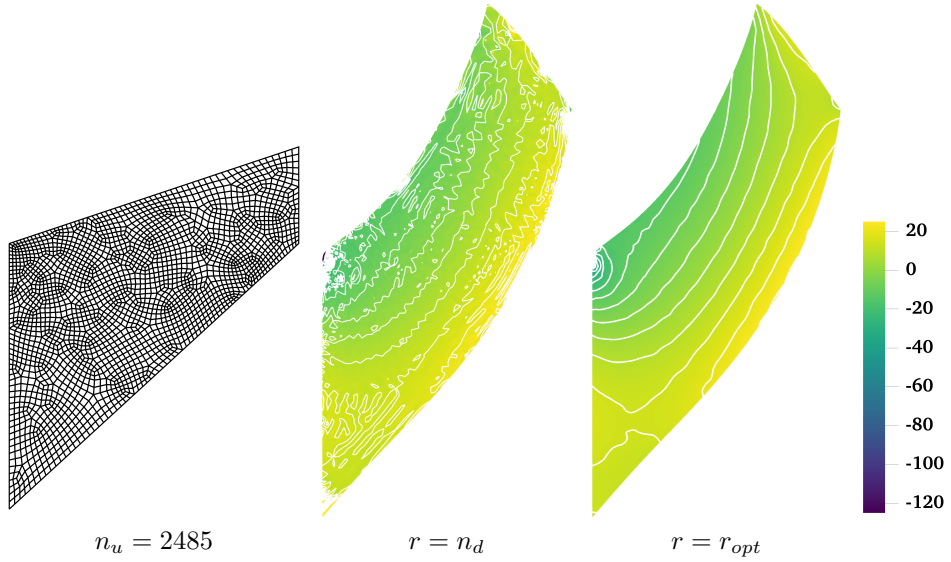


Figure 15: Comparison of pressure contour plots for Cook membrane problem with Quad4–RK

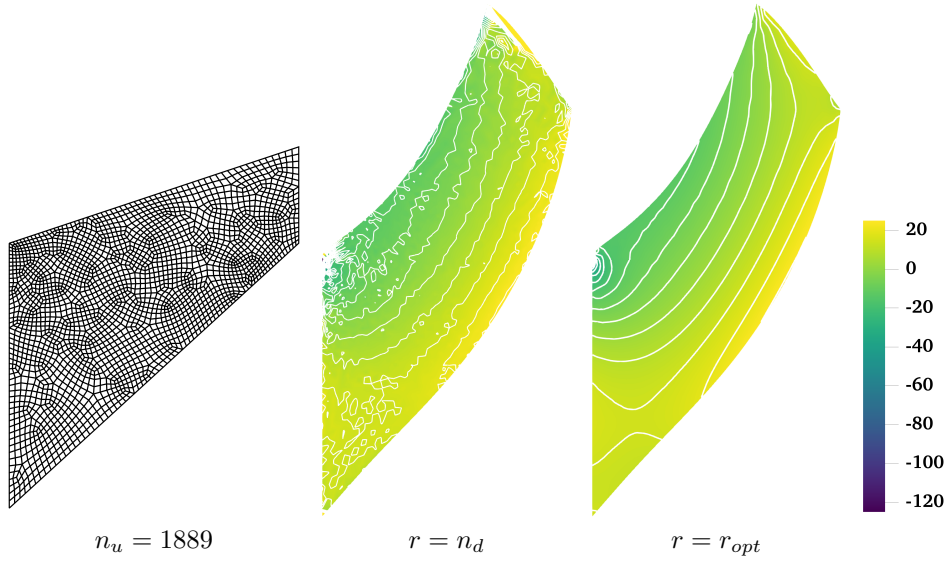


Figure 16: Comparison of pressure contour plots for Cook membrane problem with Quad8–RK

<sup>422</sup> *5.4. Block with pressure problem*

<sup>423</sup> The incompressible block problem shown in Figure 17 is considered for test-  
<sup>424</sup> ing 3D mixed formulations. The block’s dimensions are  $2L \times 2L \times L$ ,  $L = 1$ . At

425 the center of the top surface of the block is applied a pressure load  $P = 1$  with  
 426 the area of  $L \times L$ . Due to the symmetry of this problem, only a quarter model  
 427 is considered. The Young's modulus and Poisson's ratio are set as  $E = 3 \times 10^6$   
 428 and  $\nu = 0.5 - 10^{-8}$ , respectively.

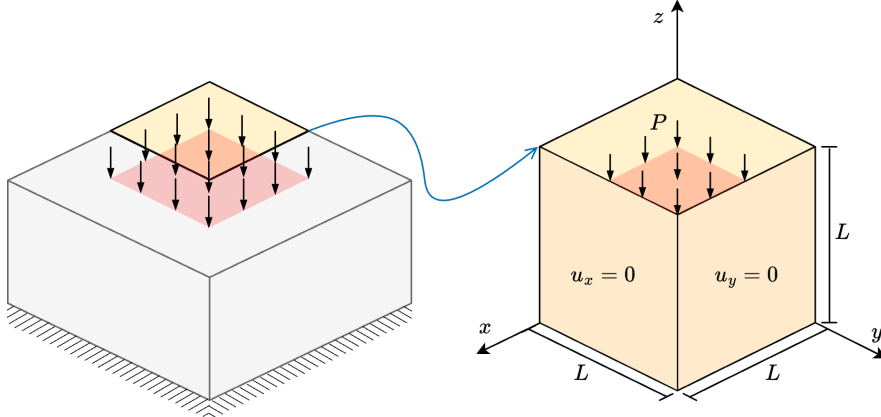


Figure 17: Illustration of block under compression problem

429 Figures study the pressure stability of 3D mixed FE-meshfree formulations,  
 430 Tet4-RK and Hex8-RK, with non-uniform nodal distribution, while the pres-  
 431 sure is discretized by linear meshfree approximations with a characterized sup-  
 432 port size of 1.5. The corresponding results also show the well performance of  
 433 the proposed optimal constraint ratio  $r = r_{opt}$ . The mixed formulations with  
 434 the traditional constraint ratio  $r = n_d$  show comparable displacement results,  
 435 but exhibit significant pressure instability.

## 436 6. Conclusion

437 This paper proposes a novel optimal constraint ratio derived from the inf-sup  
 438 condition to address volumetric locking. The optimal constraint ratio requires  
 439 that, for a given number of displacement DOFs, the number of pressure DOFs  
 440 should remain below a stabilized number determined by the proposed inf-sup  
 441 value estimator. For well-posed nodal distribution, simply counting the dis-  
 442 placement and pressure DOFs can determine whether the formulation satisfies  
 443 the inf-sup condition. Compared to the traditional constraint ratio, the pro-  
 444 posed ratio is theoretically grounded in the inf-sup condition and thus is more  
 445 precise.

446 To implement this constraint ratio, a mixed finite element (FE) and meshfree  
 447 formulation is developed. Displacements are discretized using 3-node and 6-node  
 448 triangular elements, 4-node and 8-node quadrilateral elements in 2D, and 4-node  
 449 tetrahedral and 8-node hexahedral elements in 3D. Correspondingly, linear and  
 450 quadratic reproducing kernel meshfree approximations are used for pressure

451 discretization. The reproducing kernel approximation equips globally smooth  
452 shape functions, allowing arbitrary pressure DOF placement without the limit  
453 of element.

454 Inf-sup tests for mixed FE-meshfree formulations with different constraint  
455 ratios verify the effectiveness of the proposed inf-sup value estimator. For effi-  
456 ciency and ease of implementation, the final nodal distribution scheme selects  
457 every other displacement node as a pressure node, ensuring the optimal con-  
458 straint ratio and satisfying the inf-sup condition.

459 A series of 2D and 3D incompressible elasticity examples demonstrate the  
460 effectiveness of the proposed mixed formulation. Results show that formulations  
461 with the optimal constraint ratio yield accurate displacement and pressure solu-  
462 tions. When the constraint ratio exceeds the optimal value, errors rise sharply  
463 to unacceptable levels, with the 8-node quadrilateral element being the only  
464 exception that maintains good displacement accuracy. Error convergence stud-  
465 ies and pressure contour plots further confirm that mixed formulations with  
466 the optimal constraint ratio achieve optimal convergence rates and effectively  
467 suppress pressure oscillations.

## 468 References

- 469 [1] F. Brezzi, M. Fortin, Mixed and Hybrid Finite Element Methods, Vol. 15 of  
470 Springer Series in Computational Mathematics, Springer, New York, NY,  
471 1991.
- 472 [2] T. J. Hughes, The Finite Element Method: Linear Static and Dynamic  
473 Finite Element Analysis, Prentice Hall, New Jersey, 2000.
- 474 [3] I. Babuška, R. Narasimhan, The Babuška-Brezzi condition and the patch  
475 test: An example, Computer Methods in Applied Mechanics and Engineering  
476 140 (1997) 183–199.
- 477 [4] K. J. Bathe, Finite Element Procedures, Prentice Hall, Englewood Cliffs,  
478 New Jersey, 1996.
- 479 [5] D. S. Malkus, Eigenproblems associated with the discrete LBB condition for  
480 incompressible finite elements, International Journal of Engineering Science  
481 19 (1981) 1299–1310.
- 482 [6] D. Chapelle, K. J. Bathe, The inf-sup test, Computers & Structures 47  
483 (1993) 537–545.
- 484 [7] F. Brezzi, K. J. Bathe, Studies of finite element procedures the inf-sup  
485 condition equivalent forms and applications.
- 486 [8] D. Gallistl, Rayleigh-Ritz approximation of the inf-sup constant for the  
487 divergence, Mathematics of Computation 88 (2019) 73–89.
- 488 [9] P. Hood, C. Taylor, Navier-Stokes equations using mixed interpolation,  
489 Finite element methods in flow problems (1974) 121–132.

- 490 [10] D. S. Malkus, T. J. Hughes, Mixed finite element methods - Reduced and  
 491 selective integration techniques: A unification of concepts, Computer Meth-  
 492 ods in Applied Mechanics and Engineering 15 (1978) 63–81.
- 493 [11] T. Shilt, R. Deshmukh, J. J. McNamara, P. J. O'Hara, Solution of nearly  
 494 incompressible field problems using a generalized finite element approach,  
 495 Computer Methods in Applied Mechanics and Engineering 368 (2020)  
 496 113165.
- 497 [12] J. C. Simo, M. S. Rifai, A class of mixed assumed strain methods and  
 498 the method of incompatible modes, International Journal for Numerical  
 499 Methods in Engineering 29 (1990) 1595–1638.
- 500 [13] M. Broccardo, M. Micheloni, P. Krysl, Assumed-deformation gradient finite  
 501 elements with nodal integration for nearly incompressible large deformation  
 502 analysis, International Journal for Numerical Methods in Engineering 78  
 503 (2009) 1113–1134.
- 504 [14] W. M. Coombs, T. J. Charlton, M. Cortis, C. E. Augarde, Overcoming vol-  
 505 umetric locking in material point methods, Computer Methods in Applied  
 506 Mechanics and Engineering 333 (2018) 1–21.
- 507 [15] S. Saloustros, M. Cervera, S. Kim, M. Chiumenti, Accurate and locking-free  
 508 analysis of beams, plates and shells using solid elements, Computational  
 509 Mechanics (Jan. 2021).
- 510 [16] C. Rodriguez, T.-H. Huang, A variationally consistent reproducing ker-  
 511 nel enhanced material point method and its applications to incompressible  
 512 materials, Computational Mechanics (2023) 1–20.
- 513 [17] J. Simo, R. Taylor, K. Pister, Variational and projection methods for the  
 514 volume constraint in finite deformation elasto-plasticity, Computer Meth-  
 515 ods in Applied Mechanics and Engineering 51 (1985) 177–208.
- 516 [18] C. R. Dohrmann, P. B. Bochev, A stabilized finite element method for the  
 517 Stokes problem based on polynomial pressure projections, International  
 518 Journal for Numerical Methods in Fluids 46 (2004) 183–201.
- 519 [19] C. Lovadina, F. Auricchio, On the enhanced strain technique for elasticity  
 520 problems, Computers & Structures 81 (2003) 777–787.
- 521 [20] K.-J. Bathe, The inf-sup condition and its evaluation for mixed finite ele-  
 522 ment methods, Computers & Structures 79 (2001) 243–252.
- 523 [21] T. J. R. Hughes, Multiscale phenomena: Green's functions, the Dirichlet-  
 524 to-Neumann formulation, subgrid scale models, bubbles and the origins of  
 525 stabilized methods, Computer Methods in Applied Mechanics and Engi-  
 526 neering 127 (1995) 387–401.

- 527 [22] A. Masud, K. Xia, A Stabilized MixedFinite Element Method for Nearly  
 528 IncompressibleElasticity, *Journal of Applied Mechanics* 72 (2005) 711–720.
- 529 [23] R. Rossi, R. Zorrilla, R. Codina, A stabilised displacement-volumetric  
 530 strain formulation for nearly incompressible and anisotropic materials,  
 531 *Computer Methods in Applied Mechanics and Engineering* 377 (2021)  
 532 113701.
- 533 [24] E. Karabelas, M. A. F. Gsell, G. Haase, G. Plank, C. M. Augustin, An  
 534 accurate, robust, and efficient finite element framework with applications to  
 535 anisotropic, nearly and fully incompressible elasticity, *Computer Methods in Applied  
 536 Mechanics and Engineering* 394 (2022) 114887.
- 537 [25] T. J. R. Hughes, L. P. Franca, M. Balestra, A new finite element formulation  
 538 for computational fluid dynamics: V. Circumventing the babuška-  
 539 brezzi condition: A stable Petrov-Galerkin formulation of the stokes prob-  
 540 lem accommodating equal-order interpolations, *Computer Methods in Applied  
 541 Mechanics and Engineering* 59 (1986) 85–99.
- 542 [26] D. N. Arnold, F. Brezzi, M. Fortin, A stable finite element for the Stokes  
 543 equations, *CALCOLO* 21 (1984) 337–344.
- 544 [27] F. Auricchio, L. Beirão da Veiga, C. Lovadina, A. Reali, A stability study of  
 545 some mixed finite elements for large deformation elasticity problems, *Com-  
 546 puter Methods in Applied Mechanics and Engineering* 194 (2005) 1075–  
 547 1092.
- 548 [28] A. Quarteroni, A. Valli, *Numerical Approximation of Partial Differential  
 549 Equations*, Springer Series in Computational Mathematics, Springer,  
 550 Berlin, 1994.
- 551 [29] M. Crouzeix, P. Raviart, Conforming and nonconforming finite element  
 552 methods for solving the stationary Stokes equations I, *Revue française  
 553 d'automatique informatique recherche opérationnelle. Mathématique* 7  
 554 (1973) 33–75.
- 555 [30] U. Brink, E. Stein, On some mixed finite element methods for incompress-  
 556 ible and nearly incompressible finite elasticity, *Computational Mechanics*  
 557 19 (1996) 105–119.
- 558 [31] T. Belytschko, Y. Y. Lu, L. Gu, Element-free Galerkin methods, *Internation-  
 559 al Journal for Numerical Methods in Engineering* 37 (1994) 229–256.
- 560 [32] W. K. Liu, S. Jun, Y. F. Zhang, Reproducing kernel particle methods,  
 561 *International Journal for Numerical Methods in Fluids* 20 (1995) 1081–  
 562 1106.
- 563 [33] S. W. Chi, J. S. Chen, H. Y. Hu, A weighted collocation on the strong form  
 564 with mixed radial basis approximations for incompressible linear elasticity,  
 565 *Computational Mechanics* 53 (2014) 309–324.

- 566 [34] L. Wang, Z. Qian, Y. Zhou, Y. Peng, A weighted meshfree collocation  
 567 method for incompressible flows using radial basis functions, *Journal of*  
 568 *Computational Physics* 401 (2020) 108964.
- 569 [35] A. Ortiz-Bernardin, M. Puso, N. Sukumar, Improved robustness for nearly-  
 570 incompressible large deformation meshfree simulations on Delaunay tes-  
 571 sellations, *Computer Methods in Applied Mechanics and Engineering* 293  
 572 (2015) 348–374.
- 573 [36] T. J. Hughes, J. A. Cottrell, Y. Bazilevs, Isogeometric analysis: CAD,  
 574 finite elements, NURBS, exact geometry and mesh refinement, *Computer*  
 575 *Methods in Applied Mechanics and Engineering* 194 (2005) 4135–4195.
- 576 [37] F. Auricchio, L. Beirão da Veiga, C. Lovadina, A. Reali, The importance  
 577 of the exact satisfaction of the incompressibility constraint in nonlinear  
 578 elasticity: Mixed FEMs versus NURBS-based approximations, *Computer*  
 579 *Methods in Applied Mechanics and Engineering* 199 (2010) 314–323.
- 580 [38] A. Huerta, S. Fernández-Méndez, Locking in the incompressible limit for  
 581 the element-free Galerkin method, *International Journal for Numerical*  
 582 *Methods in Engineering* 51 (2001) 1361–1383.
- 583 [39] J. Dolbow, T. Belytschko, Volumetric locking in the element free Galerkin  
 584 method, *International Journal for Numerical Methods in Engineering* 46  
 585 (1999) 925–942.
- 586 [40] G. Moutsanidis, J. J. Koester, M. R. Tupek, J.-S. Chen, Y. Bazilevs, Treat-  
 587 ment of near-incompressibility in meshfree and immersed-particle methods,  
 588 *Computational Particle Mechanics* 7 (2020) 309–327.
- 589 [41] G. Moutsanidis, W. Li, Y. Bazilevs, Reduced quadrature for FEM, IGA  
 590 and meshfree methods, *Computer Methods in Applied Mechanics and En-*  
 591 *gineering* 373 (2021) 113521.
- 592 [42] Z.-Y. Wang, Y.-F. Jin, Z.-Y. Yin, Y.-Z. Wang, Overcoming volumetric  
 593 locking in stable node-based smoothed particle finite element method with  
 594 cubic bubble function and selective integration, *International Journal for*  
 595 *Numerical Methods in Engineering* 123 (2022) 6148–6169.
- 596 [43] J. S. Chen, S. Yoon, H. P. Wang, W. K. Liu, An improved reproducing  
 597 kernel particle method for nearly incompressible finite elasticity, *Computer*  
 598 *Methods in Applied Mechanics and Engineering* 181 (2000) 117–145.
- 599 [44] C. M. Goh, P. M. F. Nielsen, M. P. Nash, A stabilised mixed mesh-  
 600 free method for incompressible media: Application to linear elasticity and  
 601 Stokes flow, *Computer Methods in Applied Mechanics and Engineering* 329  
 602 (2018) 575–598.

- 603 [45] D. S. Barbat, M. Agrawal, S. S. Gautam, A. Nandy, Hellinger–Reissner  
604 principle based stress–displacement formulation for three-dimensional iso-  
605 geometric analysis in linear elasticity, Computer Methods in Applied Me-  
606 chanics and Engineering 394 (2022) 114920.
- 607 [46] A. Huerta, Y. Vidal, P. Villon, Pseudo-divergence-free element free  
608 Galerkin method for incompressible fluid flow, Computer Methods in Ap-  
609 plied Mechanics and Engineering 193 (2004) 1119–1136.
- 610 [47] C. Wu, W. Hu, J. Chen, A meshfree-enriched finite element method for  
611 compressible and near-incompressible elasticity, International Journal for  
612 Numerical Methods in Engineering 90 (2012) 882–914.
- 613 [48] E. Stein, R. de Borst, T. J. R. Hughes (Eds.), Encyclopedia of Compu-  
614 tational Mechanics, John Wiley, Chichester, West Sussex, 2004.
- 615 [49] I. Babuška, J. Osborn, Eigenvalue Problems, in: Handbook of Numerical  
616 Analysis, Vol. 2 of Finite Element Methods (Part 1), Elsevier, 1991, pp.  
617 641–787.
- 618 [50] K. Yosida, Functional Analysis, 6th Edition, Classics in Mathematics,  
619 Springer-Verlag, Berlin Heidelberg, 1995.
- 620 [51] S. Timoshenko, J. Goodier, Theory of Elasticity, Engineering Mechanics  
621 Series, McGraw-Hill, 1969.